

Modelling the bicycle rider as a controller

Literature Review

C. Christoforidis



MODELLING THE BICYCLE RIDER AS A CONTROLLER

LITERATURE REVIEW

by

C. Christoforidis

in partial fulfillment of the requirements for the degree of

Master of Science
in Biomedical Engineering

at the Delft University of Technology.

Student number: 4737822
Project duration: 2018 – 2019
Supervisor: Dr. ir. A.L. Schwab, TU Delft
Thesis committee: Dr. ir. R. Happee, TU Delft
MSc. G. Dialynas, TU Delft

This thesis is confidential and cannot be made public until May, 2019.

©2019
C. Christoforidis

ALL RIGHTS RESERVED An electronic version of this thesis is available at
<http://repository.tudelft.nl/>.

ABSTRACT

Bicycle riding is a fundamental part of everyday transportation in many countries around the world. Ever since the development of the safety bicycle, the bicycle remains one of the most prominent means of transport. Despite cycling's prominence in every day life for almost two centuries we still do not fully understand how the rider controls the bike in a more systematic way.

The purpose of this literature study is to explore and evaluate models of the single track vehicle rider found in the researched bibliography. Firstly a brief analysis of bicycle stability and its dynamics is presented as explored by Meijaard et al.[12]. In Chapter ??models which were classified on their control theory approach are presented. In section ??, models using the classical control approach are described. Following the steps of early cybernetics research in which airplane pilot modelling was pioneered by McRuer[9–11], a plethora of authors attempted adapting McRuers crossover model in order to model the rider of a seemingly much more complex task, motorcycle and bicycle riding. However some argued that such an approach will not work since cycling is not just a compensatory task. These spawned a new wave of research focusing in optimal control which is described in section ?? . This approach has its roots in early motor control research in which the human brain is believed to work as a constrained optimal controller. In the final section of Chapter ??, all models that do not fall under the two approaches described above are reviewed. These include fuzzy logic controllers which have the advantage of incorporating heuristic findings that are impossible to formulate using systematic mathematical approaches. Also intermittent control is briefly explored as a solution.

Based on this literature review the graduation project will try to model the human controller for bicycles, while focusing on the roll stabilization task. Open road experiments will be conducted in effort to estimate the controller's parameters and indirectly validate it with real cycling data.

*C. Christoforidis
Delft, April 2018*

CONTENTS

1	Introduction	1
2	A gray box analysis of the effect of torque feedback during cycling under lateral perturbations	3
2.1	Introduction	3
2.2	Methods	3
2.2.1	Bicycle Model	3
2.2.2	Rider Control Model	5
2.2.3	Parameter Estimation	6
2.3	Results	7
2.3.1	Zero Delay Model	7
2.3.2	Variable Delay Model	8
2.3.3	Final Model	9
2.4	Conclusions	11
A	Calibration of Inertial Measurements	19
B	Orientation Estimation from Inertial Measurements	23
B.1	Offline Estimation Methods	23
B.2	Online Estimation Methods	24
C	Estimation of Rider Torque	29
C.1	Steer rate and acceleration	29
C.2	Steering shaft moment of inertia and viscous friction	29
C.3	Motor Torque Input Validation	32
C.3.1	Design of torque sensor	32
C.3.2	Results	33
Bibliography		37

1

INTRODUCTION

Bicycle riding is a fundamental part of everyday transportation in many countries around the world. Ever since the development of the safety bicycle(two equal sized wheels, pneumatic tires, chain drive, rear wheel propulsion and a bent front fork), almost 130 years ago, the bicycle remains one of the most prominent means of transport [7]. With the growing concerns of sedentary lifestyles many choose the bicycle as their primary commute vehicle with the hopes of maintaining some levels of fitness. Additionally the bicycle is the preferred means of physical exercise for the elderly especially in the Netherlands and Denmark. Despite the fact that riding a bicycle is one of the first skills we acquire as kids and is used throughout the adult life, the fundamental way humans control the bicycle and ,generally single track vehicles, is yet to be understood.

In a recent study examining the entries of patients to the emergency department due to traffic related accidents in the Netherlands (see Fig. C.3), it was found that bicycle related accidents were the most prevalent. With over 60,000 reported cases bicycle accidents outnumber automobile accidents more than 4 to 1. It therefore becomes clear that a lot could be done to improve cycling safety. Further look at the figure will reveal that most of those accidents did not involve a second party. There was just a rider that fell off his bike. Although there are several potential reasons that riders lose control of the bicycle, formulating a general model of how humans control single track vehicles could prove invaluable in understanding the causes behind the above numbers.

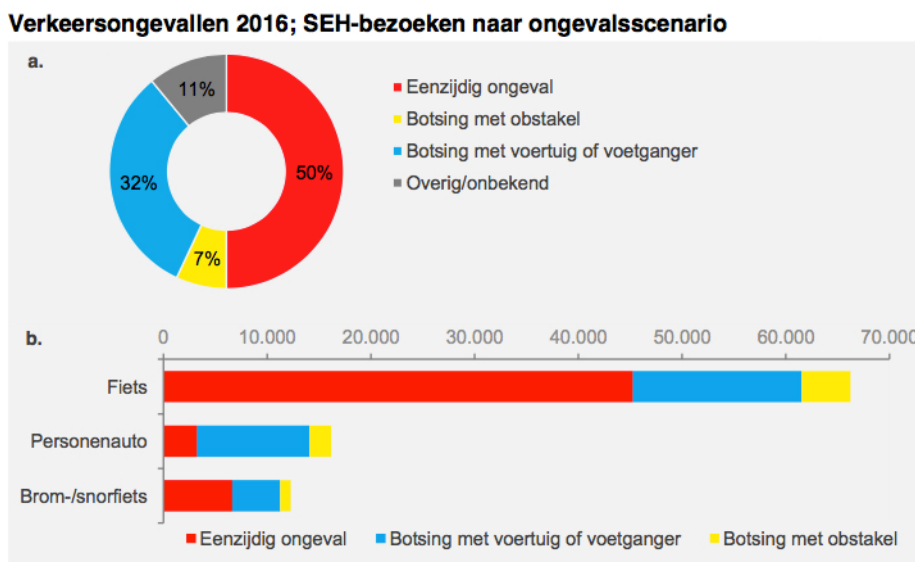


Figure 1.1: The number of road users that visit the emergency department at a hospital after a traffic accident in the Netherlands in 2016. Red indicates single vehicle accidents, yellow indicates a collision with an obstacle, blue indicates multi-vehicle accident and grey indicates other type of accidents[8].

Every human-machine system requires an understanding of how the plant operates. In the case of the bicycle multiple efforts have been made in capturing the dynamics of the bicycle and its self-stabilizing behavior. These have resulted in a set of linearized equations of motion, now commonly referred to as the Whipple Carvalho model [12], which is going to be discussed further in chapter ??.

As it is known single track vehicles are not stable at low speeds. This is why a controller (like the human rider) is required to close the loop and create a stable system. There are two ways with which the human affects the dynamics of the plant. The first is with its passive interactions with the plant as a physical multi-body system. Most passive models model the rider as a point mass rigidly attached to the rear frame, or as a pendulum connected to the rear frame [4], although recent efforts have been made to extend this further with more complex passive rider models which include modeling of neuromuscular dynamics with spring-damper systems at various interfaces between rider and the bicycle frame[5]. The second is with its active control behavior. This involves the active control motion, such as steering, leaning or pedaling, applied by the rider to control and balance the bicycle. In most such cases, the passive behavior of the rider is simplified by only accounting for a fixed mass on the seat post, but when lean torque needs to be examined more complex modeling is required. The focus of the study is to explore the available models that best express the human rider as a controller in the bicycle-rider closed loop system.

The literature review presented herein gives an overview of research done in the field of active rider modelling concerning single-track vehicles, while discussing with which methods and to what extent have these models been validated. This extensive overview is given in section ?? of chapter ??, which is structured in three sections: ?? Classical control system design, ?? Optimal control system design and ?? Other control system design. Chapter ?? concludes on the results from Chapter ?? having as a final goal to answer the research question:

- **What is the controller that best simulates the behavior of the human in the control of single track vehicles?**

2

A GRAY BOX ANALYSIS OF THE EFFECT OF TORQUE FEEDBACK DURING CYCLING UNDER LATERAL PERTURBATIONS

2.1. INTRODUCTION

2.2. METHODS

2.2.1. BICYCLE MODEL

The bicycle model used is the so called Whipple-Carvalho model the dynamics of which have been expressed in a set of linearized equations by Meijaard et al. [12]. In the original model three assumptions are made. The first is that the rider is rigidly attached in the saddle with the mass of the arms and legs acting as a point. Secondly, the contact between tire and ground is modelled as a non slipping rolling point contact meaning that the wheels can rotate without lateral slip. Lastly it is assumed that the total energy of the system is preserved. The resulting non-holonomic mechanical model has three velocity degrees of freedom, the forward speed, the rear frame roll rate ϕ and the steering rate δ . The lateral motion is described by two coupled second order

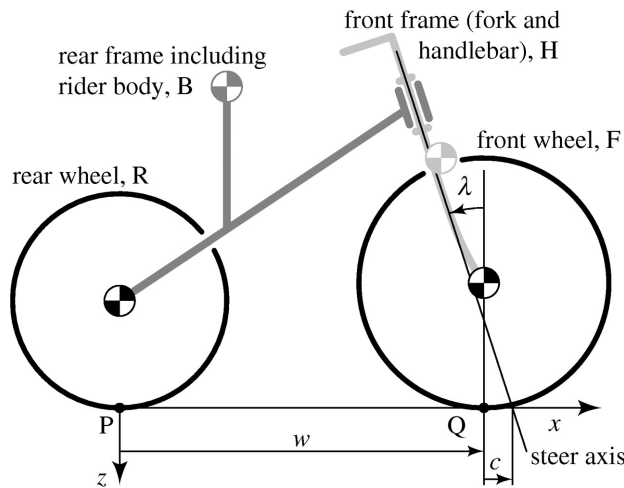


Figure 2.1: The Whipple-Carvalho bicycle model consists of four rigid bodies: rear wheel R, rear frame B, front frame H and front wheel F connected via hinges. The center of mass locations are expressed relative to the x - and z -coordinates shown (with origin at P and y pointing towards the reader). The other parameters shown are the steer axis tilt λ , wheelbase w and trail c . The model at its most expanded form is described by 25 parameters.[12]

differential equations given by equation (2.1).

$$\mathbf{M}\ddot{\mathbf{q}} + \nu\mathbf{C}_1\dot{\mathbf{q}} + [\mathbf{gK}_0 + \nu^2\mathbf{K}_2]\mathbf{q} = \mathbf{f} \quad (2.1)$$

where \mathbf{q} is a vector containing the roll and steer angles, \mathbf{f} is a vector containing the roll and steer torques, g is the gravitational acceleration and \mathbf{M} , $v\mathbf{C}_1$, $g\mathbf{K}_0 + v^2\mathbf{K}_2$ are the "mass", "damping" and "stiffness" ratios in matrix form respectively. The entries in the constant coefficient matrices $\mathbf{M}, \mathbf{C}_1, \mathbf{K}_0, \mathbf{K}_2$ are calculated from a set of 25 bicycle parameters related to inertial and design properties of the steer by wire bicycle (see table 2.4).

To determine the stability of the open loop system in a straight ahead motion the characteristic polynomial derived from

$$\det(\mathbf{M}\lambda^2 + v\mathbf{C}_1\lambda + g\mathbf{K}_0 + v^2\mathbf{K}_2) = 0 \quad (2.2)$$

is solved for a forward speed range from 0 to 10 m s⁻¹ where λ are the eigenvalues of the system (see figure 2.2). The two interesting eigenmodes defined by the locus plot are the weave and capsizing. The weave corresponds to an oscillatory mode as can be seen by the existence of imaginary parts and represents a motion in which the bicycle sways about its heading. The oscillatory motions exponentially fades when forward speed is larger than 4.39 m s⁻¹. The capsizing on the other hand has an eigenvector dominated by lean and leads to a gradual roll drift to infinity when the eigenvalue crosses the zero line around 6.67 m s⁻¹. Since in the experimental

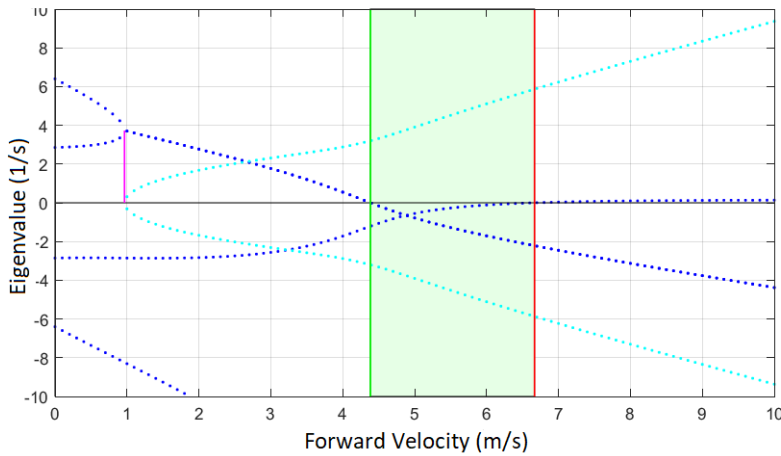


Figure 2.2: Root locus plot of the steer by wire bicycle. Dotted blue lines indicate the real part of the eigenvalues while dotted cyan show the imaginary part. The stable region corresponds to speeds $4.39 \lesssim v \lesssim 6.67 \text{ ms}^{-1}$

setup the task could not be isolated to purely balance the equations are extended to include heading. Heading is defined as a linear combination of steer angle and steer rate as expressed by Meijaard et al. [12] in equation (2.3). Additionally, the bike is assumed to be controlled only by a steering torque because according to both Moore [14] and Weir [18] the rear frame roll angle is mainly controlled by steering.

$$\dot{\psi} = \frac{v\delta + c\dot{\delta}}{w} \cos \lambda \quad (2.3)$$

When modelling the feedback off case of the steer-by-wire bicycle the dynamics of the plant need to change accordingly. In that configuration the forcing steering input is directly proportional to steering acceleration times the inertia of upper handlebar assembly, for this reason the second of the set of equations in 2.1 is replaced by:

$$I_{F_{xx}}\ddot{\delta} = T_\delta \quad (2.4)$$

For control purposes equation (2.1) is expressed in state space form with state vector $\mathbf{x} = [\dot{\phi}, \dot{\delta}, \phi, \delta, \psi]^T$, forcing input $\mathbf{f} = T_\delta$ and output equal to the full state.

$$\dot{\mathbf{x}} = \mathbf{A}\mathbf{x} + \mathbf{B}T_\delta + \mathbf{H}w \quad (2.5)$$

$$\mathbf{y} = \mathbf{C}\mathbf{x} + \mathbf{D}\mathbf{f} \quad (2.6)$$

where matrices A, B, C, D are defined by:

$$\mathbf{A} = \begin{bmatrix} -\mathbf{M}^{-1}\nu\mathbf{C}_1 & -\mathbf{M}^{-1}(g\mathbf{K}_0 + \nu^2\mathbf{K}_2) \\ \mathbf{I}_2 & \mathbf{0} \\ 0 & \frac{c\cos\lambda}{w} \end{bmatrix}, \mathbf{B} = \begin{bmatrix} \mathbf{M}^{-1} \\ \mathbf{0} \end{bmatrix} \quad (2.7)$$

$$\mathbf{C} = \mathbf{I}_5, \mathbf{D} = \mathbf{0} \quad (2.8)$$

where \mathbf{H} is the matrix defining the dynamics of the lateral disturbance w .

2.2.2. RIDER CONTROL MODEL

In order to investigate the effects of the torque feedback loop attributed to the golgi tendon organs a rider control model is created. The complete high level overview of the model is shown in figure 2.3.

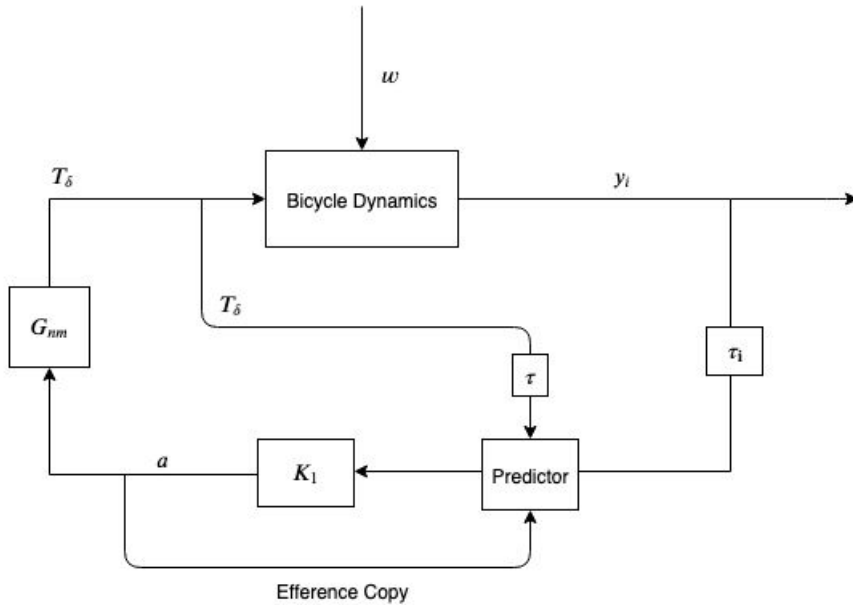


Figure 2.3: Block diagram of the complete rider-bicycle model. G_{nm} is the neuromuscular dynamics block. K_1 is a pure Gain block working on the extended output plus the torque feedback while τ_i are the delays of each output y_i attributed to different sensory organs of the human body.

G_{nm} is the neuromuscular transfer function and works as a second order filter to simulate the limitations of the human response. In state space form this block is expressed by:

$$\dot{x}_{nm} = \begin{bmatrix} 0 & 1 \\ -\omega_c^2 & -2\zeta\omega_c \end{bmatrix} \begin{bmatrix} T_\delta \\ \dot{T}_\delta \end{bmatrix} + \begin{bmatrix} 0 \\ \omega_c^2 \end{bmatrix} a \quad (2.9)$$

$$y_{nm} = [1 \ 0] \begin{bmatrix} T_\delta \\ \dot{T}_\delta \end{bmatrix} \quad (2.10)$$

where ζ is the damping coefficient and ω_c is the cutoff frequency. These parameters were chosen according to activations dynamics present in the shoulder joint [6].

The steer angle and steer rate feedback is attributed to the muscle spindles, while the torque feedback is made possible with the help of the golgi tendon organs. The roll and heading angle come from the visual system. Lastly the roll rate feedback is attributed to the vestibular system.

The bicycle model of equation (2.5) is combined with the neuromuscular dynamics block of equation (2.10) to create a combined plant with state $x = [\dot{\phi}, \dot{\delta}, \phi, \delta, \psi, T_\delta, \dot{T}_\delta]^T$, input a and w and output $y = [\dot{\phi}, \dot{\delta}, \phi, \delta, \psi, T_\delta]^T$. In order to make possible the implementation of the predictor which is discrete in nature the state space representation of the combined plant is discretized with a time step of 0.001 s. The equivalent model block diagram is shown in figure 2.4.

THE REAFFERENT OPTIMAL PREDICTOR

Many strategies to counter time delays have been proposed in literature. The most basic predictor is the Smith Predictor, which has been explored in motor control research by Miall et al. [13]. The smith predictor compensates for time delays through the use of an internal forward model of the controlled dynamics and an internal model of the sensory delay pathways. The forward model works by utilizing an efferent signal of the control input while the comparison between prediction and measurement is trying to simulate the human's ability to distinguish between reafference and exafference. Unfortunately the most basic smith predictor scheme does not work for unstable open loop systems [?]. In this work a modification to the normal smith predictor scheme is suggested. In place of the forward model an optimal tapped delay line is used that forward simulates the amount of steps according to the model of sensory delay. This works like a re-setting forward model that is updated every time step by the delayed state so the predictor loop does not become unstable. A tapped delay line without the smith correction can still work and has been implemented by van der Kooij et al. [17] for modelling stance control but it leads to predictions that do not contain any amount of the effect of the disturbance on the state. The predictor structure used in this work can be seen in figure 2.4.

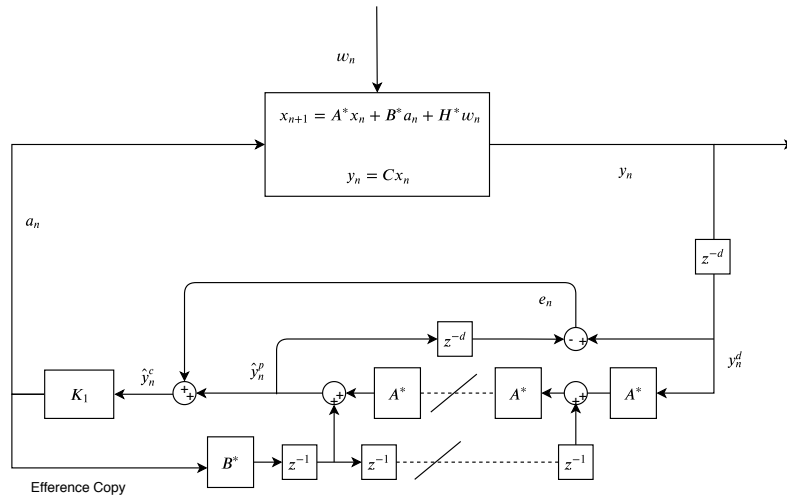


Figure 2.4: Equivalent block diagram of the bicycle-rider system in discrete time. A^* , B^* are the discretized matrices of the combined plant dynamics while d is the amount of time delay in number of time steps. The delayed output measurement is forwarded in time in the tapped delay line to produce the first undelayed estimate of the output \hat{y}^P , which is again delayed through a model of the time internal time delay. The difference between this re-delayed prediction with the delayed measurements creates the error e which is added back to \hat{y}^P to create the final corrected prediction \hat{y}^C

2.2.3. PARAMETER ESTIMATION

In order to assess the effectiveness of the torque feedback loop, three models of incremental complexity are used. In the first the feedback pathways are fed into the controller without delays. In the second delays are added. The third one compensates for time delays by the use of the predictor described above. The three models have the controller gains as free parameters. The gains are estimated by fitting the model output into the non-parametric dataset derived in [3]. The gains were estimated by minimization of the cost function

$$V_N(\theta) = \frac{1}{N} \sum_{k=1}^N \left[5 \cdot (\hat{y}_k^\delta(\theta) - y_k^\delta)^2 + (\hat{y}_k^\psi(\theta) - y_k^\psi)^2 + 8 \cdot 10^{-4} (\hat{y}_k^{T\delta}(\theta))^2 \right] \quad (2.11)$$

where θ is a vector containing all the free parameters, \hat{y}^δ and \hat{y}^ψ are the outputs of the simulation for the measured external disturbance w and the vector of parameters θ for steer angle and heading angle respectively, while y^δ and y^ψ are the outputs of the convolution of the measured disturbance w and the impulse response functions h^δ and h^ψ respectively.

The first two terms of the cost function are trying to match the steering and heading response of the parametric model with that one of the non-parametric model, while the third one minimizes the amount of input torque generated in order to produce the best possible fit. The weights were chosen heuristically. For optimization the genetic algorithm with a fitness limit of 0.03 is first used in order to produce a good starting parameter vector for gradient descend algorithm to take over, which finally finds the closest possible estimate of the global minimum. For the genetic algorithm a crossover fraction of 0.85 along with a population size 10 times the length of the parameter vector is used. Additionally, the gains attributed to the muscle spindle sensors (K_δ and $K_{\dot{\delta}}$) are constrained to be only positive. The assumption is that they work like a delayed steering stiffness and damping.

The impulse response function of the median rider is used. This is determined by taking the mean impulse response function of each measured output and finding the participant which had the highest variance accounted for between the individual response and the mean across all speed levels. Each system was identified for three different model conditions. In the first all six feedback pathways are used including torque feedback, on the second torque feedback is excluded from the model by assuming that its corresponding gain is zero. Finally in the third, six gains are again used but the plant dynamics are modified so as to simulate the feedback off case of the experimental condition as described in section 2.2.2. As metric of model validity the variance accounted for between parametric and non-parametric output is used, defined as

$$\text{VAF}_d(\boldsymbol{\theta}) = 1 - \sum_{k=1}^n \left(y^d(k) - \hat{y}^d(k, \boldsymbol{\theta}) \right)^2 / \sum_{k=1}^n \left(y^d(k) \right)^2 \quad (2.12)$$

where $d = \{\phi, \delta, \psi\}$.

In order to assess the importance of the torque feedback, the uncertainty of each parameter is found. Parameters with the lowest uncertainty contribute more to the fit so they are deemed more important. To find the uncertainty the covariance matrix is estimated from :

$$\text{cov}_{\hat{\theta}} = V_N(\hat{\boldsymbol{\theta}}) \mathbf{H}(\hat{\boldsymbol{\theta}})^{-1} \quad (2.13)$$

$$\text{with } \mathbf{H}(\hat{\boldsymbol{\theta}}) = \frac{\partial^2 V_N}{\partial \theta_i \partial \theta_j} \quad (2.14)$$

where $\hat{\boldsymbol{\theta}}$ is the parameter vector that produces the closest estimate to the global minimum and \mathbf{H} is the hessian matrix numerically estimated by the gradient descend algorithm. However, since bigger parameters are going to have naturally larger variances the diagonal values are normalized by the parameter value to produce the index of dispersion

$$D_{\hat{\theta}_i} = \frac{\sigma_{\hat{\theta}_i}^2}{|\hat{\theta}_i|} \quad (2.15)$$

where $\sigma_{\hat{\theta}_i}^2$ are the diagonal elements of $\text{cov}_{\hat{\theta}}$.

2.3. RESULTS

2.3.1. ZERO DELAY MODEL

The results of the zero delay model are presented in table 2.1. A fit of over 90 % is easily achieved for both steer angle and heading, while for roll the discrepancy is larger. A look into how the model approximates the measured rider input and bicycle states for the forward speed 3.6ms^{-1} is seen in figure 2.5. The discrepancy in the roll angle fit can be explained by the fact that the model does not account for upper body motions which are expected to have a considerable impact on bicycle dynamics.

From the index of dispersion it is seen that the torque feedback gain K_{T_δ} along with the steer rate gain $K_{\dot{\delta}}$ contribute most in the fit, since they consistently have the lowest uncertainty level among all parameters. Additionally, VAF_δ drops more than 15-20% when the feedback is turned off (see table 2.1). The steering angle response becomes significantly more oscillatory when the feedback is turned off (see figure 2.6). Roll stabilization performance does not seem to be affected, however steering effort considerably does. Worth noting that in the experimental feedback off case the level of fit degradation is almost non existant.

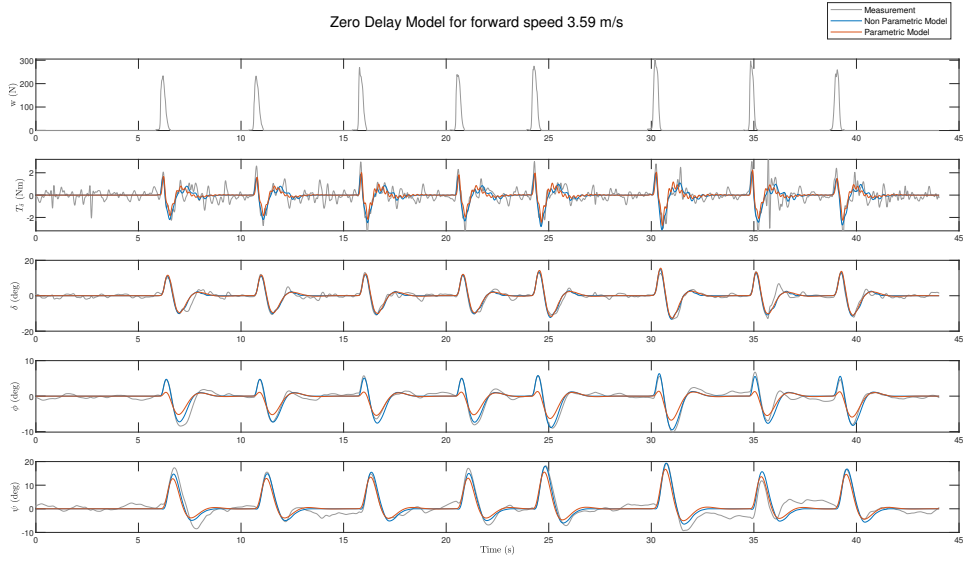


Figure 2.5: Comparison between parametric model output, non-parametric model output and measured signals for the speed level of 3.6 m s^{-1} for the case where torque feedback activated.

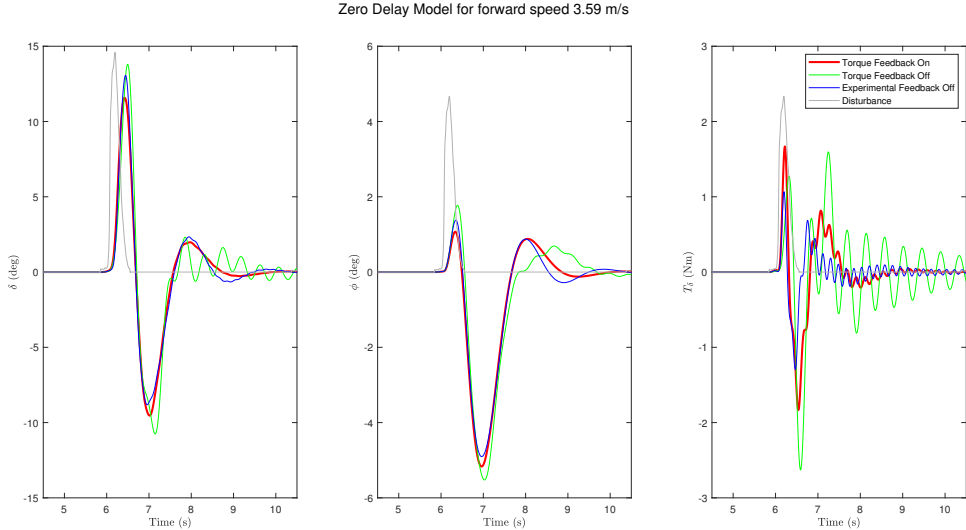


Figure 2.6: Steering, roll angles and input rider torque compared among torque feedback levels for the forward speed of 3.6 m s^{-1} . The disturbance signal is not shown to scale.

2.3.2. VARIABLE DELAY MODEL

The same procedure was repeated for the model but now introducing delays in all feedback pathways. For δ and $\dot{\delta}$ which are attributed to the muscle spindle sensors and for the torque feedback which is attributed to the golgi tendon organs a delay of 25 ms is chosen [2, 16]. For the feedback states attributed to visual feedback such as the roll angle ϕ and yaw angle ψ a much greater delay of 200 ms is chosen. Finally for the vestibular roll rate feedback a delay of 50 ms is implemented [1].

The results of the variable delay model are presented in table 2.2. Despite the fact that significant delay is introduced into the system the torque feedback loop manages to compensate maintaining a VAF_δ of over 90 % for low speed levels (see table 2.2 and figure 2.7). In figure 2.8 the delayed response of the rider is visible between the dotted red and bold red line. This is further exaggerated in the two remaining conditions resulting in much more oscillatory steering responses with a visible impact on roll stabilization. The index

of dispersion follows similar pattern as in the zero delay model, with the proportional heading and roll gains having the largest uncertainty while the steer rate and torque feedback gain having the lowest. Between feedback on and feedback off, a much larger drop in VAF is noted. Additionally, a equally significant drop in the fit is noted for the experimental feedback off case, which was not present in the zero delay model.

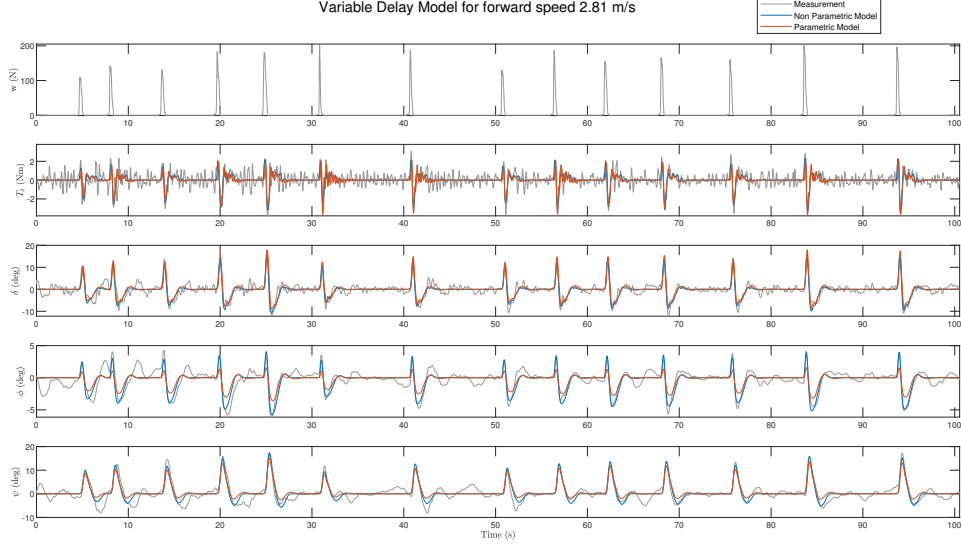


Figure 2.7: Comparison between variable delay model output, non-parametric model ouput and measured signals for the speed level of 2.8 ms^{-1} for the case where torque feedback is activated.

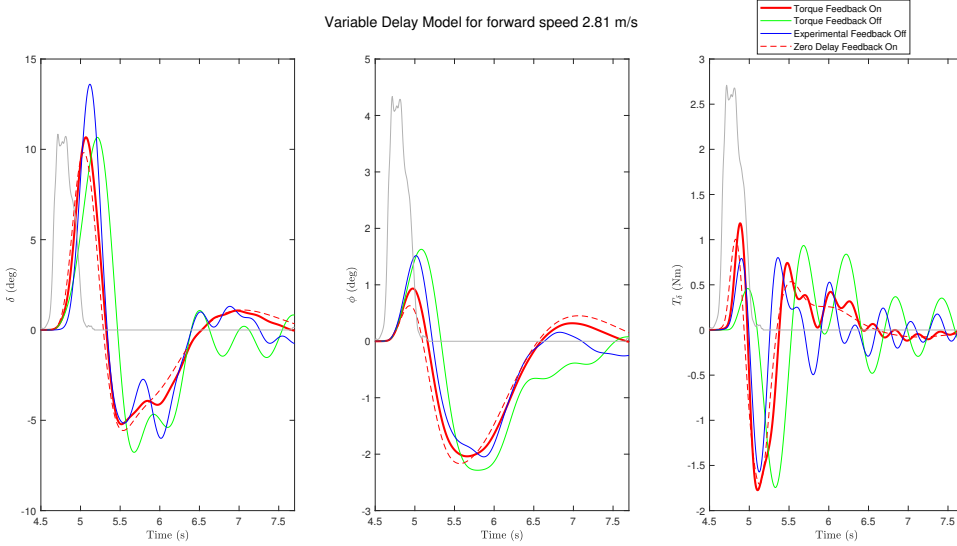


Figure 2.8: Steering, roll angles and input rider torque of the variable delay model compared among torque feedback levels for the forward speed of 2.8 ms^{-1} . The disturbance signal is not shown to scale.

2.3.3. FINAL MODEL

The final model of figure 2.4 is implemented with a consistent time delay among sensory pathways eqaul to 50 ms. Adaptation of the predictor to work with variable time delays is not part of the scope of this work. It is assumed that the internal model of bicycle and neuromuscular dynamics along with the internal model of the inherent time delay responsible for prediction is perfect for controlling the normal bicycle dynamics. However in the experimental off case the internal model is not updated in simulation, which that it remains

the same as a normal bike. This falls inline with what was noted during the experiments where the subjects adapted to the new bicycle dynamics instantaneously, so a full "recalibration" of the forward model is too far fetched. This way the extent to which the smith prediction principle can counter prediction model inaccuracies is also tested.

The optimization results for the final model are presented in table 2.3. From the VAFs and the signals shown in figure 2.9 it is visible that the quality of the fit is comparable with the ideal zero delay case. The index of dispersion follows similar trends. The drop between feedback conditions is also similar to the zero delay case. Furthermore, the steering response exhibits the same oscillatory behaviour when torque feedback is completelyley disabled. However, the predictor manages to compensate in the feedback off experimental case and achieve good fit which was not present in the model with uncompensated time delays.

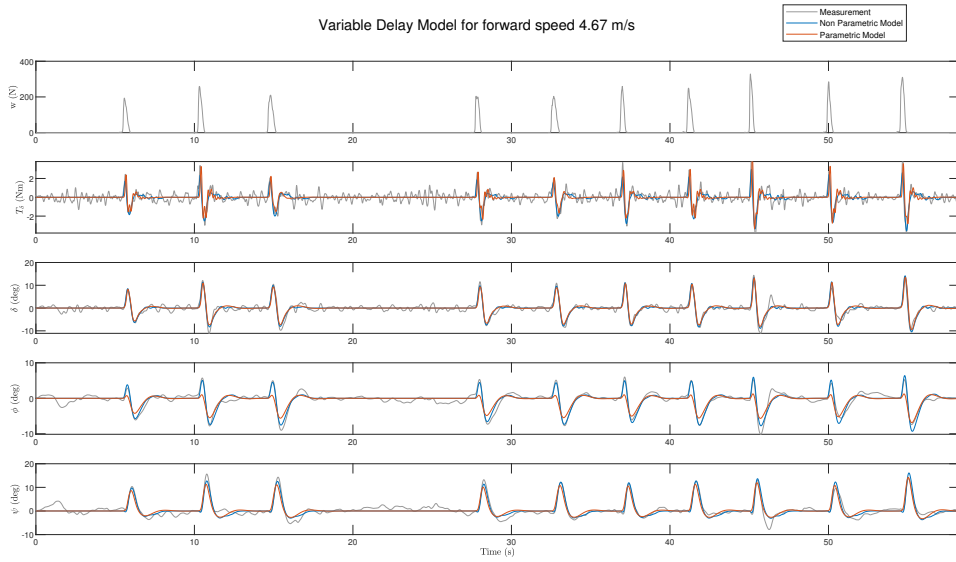


Figure 2.9: Comparison between variable delay model output, non-parametric model output and measured signals for the speed level of 4.67 ms^{-1} for the case where torque feedback is activated.

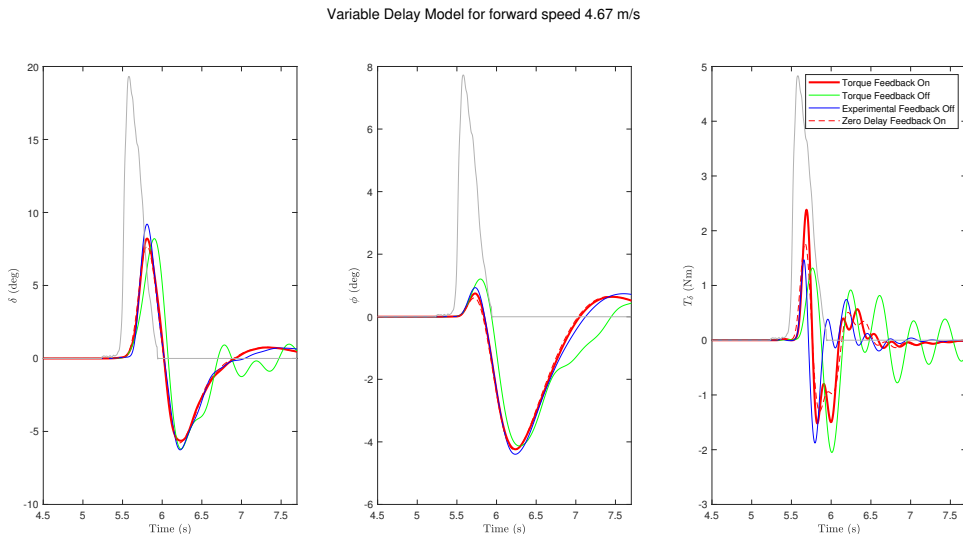
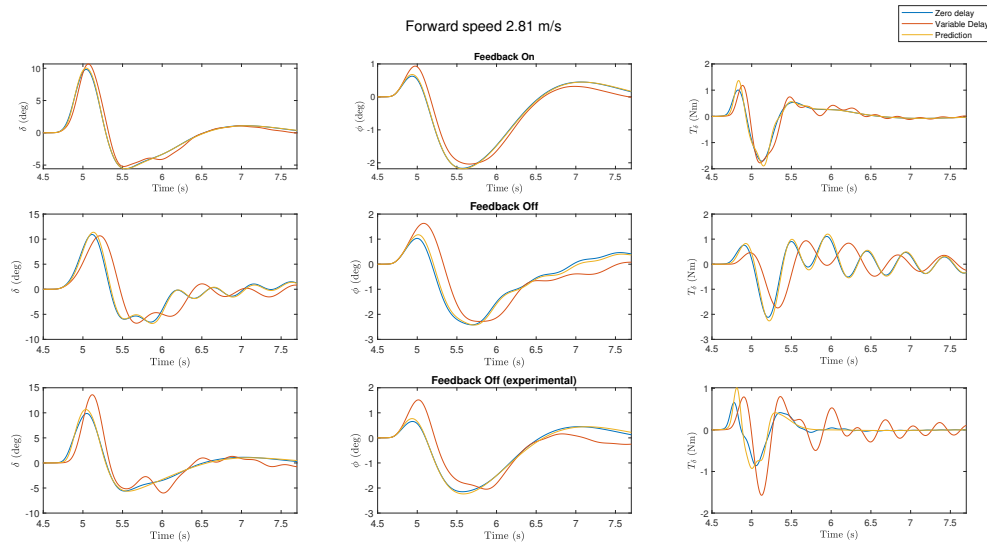


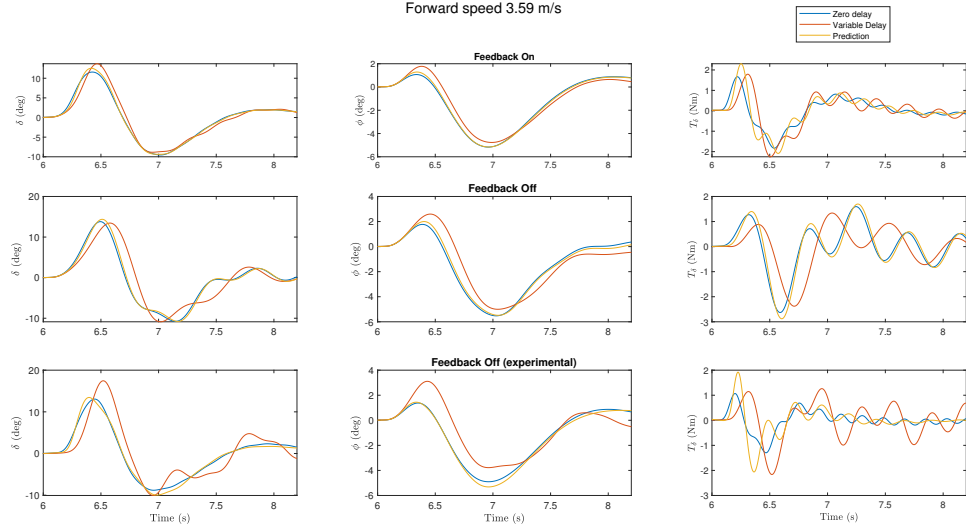
Figure 2.10: Steering, roll angles and input rider torque of the variable delay model compared among torque feedback levels for the forward speed of 4.67 ms^{-1} . The red dotted lines is the feedback on case of the zero delay model and is shown for reference. The disturbance signal is not shown to scale.

In figures 2.11 to 2.12 a complete comparison between rider models for all feedback conditions is presented. The response shown is the result of the first lateral perturbation of each individual run. The zero delay and prediction models exhibit almost identical responses as it was evident from the over 90% fit achieved. The variable delay model lags behind in both the produced control input and bicycle output, as is expected. Worth noting the lag in the control input of the prediction model in the first few milliseconds after the perturbation. Despite that fact the model compensates and achieves similar output as the idealized zero delay case. This is a result of the fact that no matter how good the prediction algorithm is the human has no knowledge of the future so the response from the controller will start after the first state information arrives from the feedback pathways which are delayed. The forward model in this case does not help predict the state as it has no information of the external disturbance.

2.4. CONCLUSIONS



(a) Comparison between the three rider models for forward speed 2.81 m s^{-1}



(b) Comparison between the three rider models for forward speed 3.6 m s^{-1}

Figure 2.11: Steering angle δ , roll angle ϕ and steering torque T_δ compared among the three rider models implemented for all torque feedback conditions, for the two lowest speed levels.

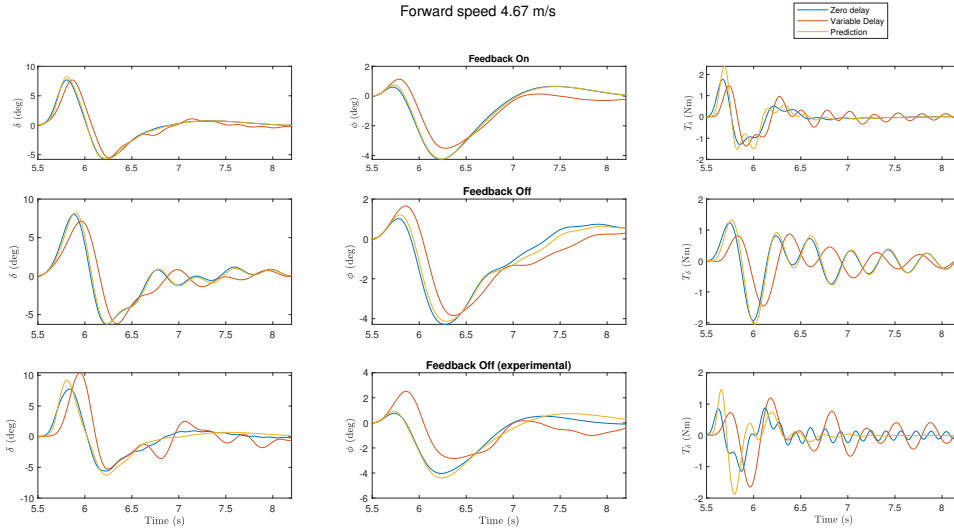
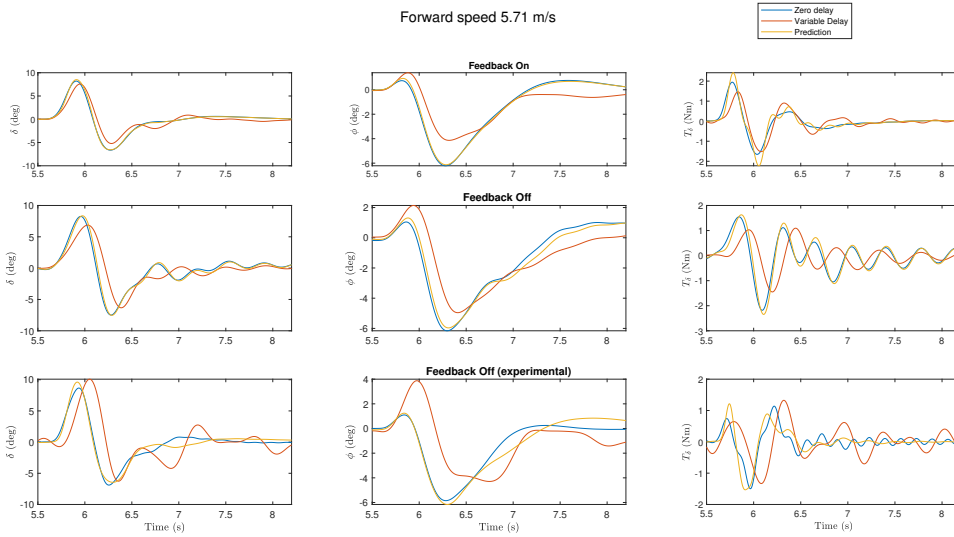
(a) Comparison between the three rider models for forward speed 4.67 ms^{-1} (b) Comparison between the three rider models for forward speed 5.71 ms^{-1}

Figure 2.12: Steering angle δ , roll angle ϕ and steering torque T_δ compared among the three rider models implemented for all torque feedback conditions, for the two highest speed levels.

Table 2.1: Results for the zero delay model as estimated for the median rider for all speed levels. Results are presented for the three conditions. Feedback on includes torque feedback in the loop while feedback off completely removes it. Feedback off (experimental) is the model response with all loops connected but with the dynamics of the plant modified to simulate the feedback off condition in the experimental setup. The values of the gains are presented as well as their corresponding uncertainty level measured by the index of dispersion D_i . Additionally, the variance accounted for of the orientation outputs between parametric and non parametric signals is also presented. The derivative gains ($K_{\dot{\phi}}, K_{\dot{\delta}}$) are measured in $\text{kg m}^2 \text{s}^{-2}$ while the proportional gains (K_ϕ, K_δ, K_ψ) are measured in $\text{kg m}^2 \text{s}^{-1}$. The torque feedback gain K_{T_δ} is dimensionless.

Forward Speed	Feedback On		Feedback Off		Feedback Off (experimental)	
	Value	$D (10^{-4})$	Value	$D (10^{-4})$	Value	$D (10^{-4})$
2.8 m s^{-1}	$K_{\dot{\phi}}$	-77.11	120.20	-22.46	1.99	-115.36
	$K_{\dot{\delta}}$	2.27	4.06	2.58	0.09	8.76
	K_ϕ	-164.65	231.94	-24.5	13.10	-248.24
	K_δ	32.65	56.73	3.76	7.47	29.67
	K_ψ	-63.16	106.66	-9.85	2.84	-93.44
	K_{T_δ}	3.5	10.52	-	-	7.53
	VAF_ϕ	77.78		82.79		78.37
	VAF_δ	98.34		79.19		98.20
	VAF_ψ	93.44		93.51		93.74
3.6 m s^{-1}	$K_{\dot{\phi}}$	-109.94	237.50	-21.30	2.76	-78.28
	$K_{\dot{\delta}}$	8.22	15.88	3.30	0.20	9.09
	K_ϕ	-248.47	539.80	-34.64	17.73	-229.14
	K_δ	50.78	110.81	6.48	11.05	53.16
	K_ψ	-132.13	305.58	-17.74	6.80	-103.75
	K_{T_δ}	4.52	12.65	-	-	6.89
	VAF_ϕ	79.92		85.93		80.89
	VAF_δ	98.83		86.40		97.08
	VAF_ψ	95.33		97.95		95.15
4.7 m s^{-1}	$K_{\dot{\phi}}$	-92.50	127.37	-27.29	5.88	-102.63
	$K_{\dot{\delta}}$	4.81	16.11	4.25	0.73	11.24
	K_ϕ	-183.03	336.73	-38.17	22.30	-249.74
	K_δ	22.57	127.32	2.65	92.80	63.36
	K_ψ	-165.42	266.33	-33.78	13.73	-188.67
	K_{T_δ}	3.42	10.37	-	-	8.98
	VAF_ϕ	77.03		83.06		78.60
	VAF_δ	97.57		80.27		95.57
	VAF_ψ	91.41		97.03		92.48
5.7 m s^{-1}	$K_{\dot{\phi}}$	-83.90	116.05	-31.12	6.02	-76.30
	$K_{\dot{\delta}}$	5.83	11.89	5.58	0.92	10.91
	K_ϕ	-166.08	271.62	-43.64	19.67	-208.33
	K_δ	14.85	14.29	1.14	385.00	79.44
	K_ψ	-186.77	308.69	-49.82	13.63	-176.96
	K_{T_δ}	3.24	11.10	-	-	8.45
	VAF_ϕ	79.17		84.03		80.30
	VAF_δ	97.51		84.09		94.71
	VAF_ψ	90.97		96.41		91.56

Table 2.2: Results for the variable delay model as estimated for the median rider for all speed levels. Results are presented for the three conditions. Feedback on includes torque feedback in the loop while feedback off completely removes it. Feedback off (experimental) is the model response with all loops connected but with the dynamics of the plant modified to simulate the feedback off condition in the experimental setup. The values of the gains are presented as well as their corresponding uncertainty level measured by the index of dispersion D_i (dimensionless). Additionally, the variance accounted for of the orientation outputs between parametric and non parametric signals is also presented. The derivative gains ($K_{\dot{\phi}}, K_{\dot{\delta}}$) are measured in $\text{kgm}^2 \text{s}^{-2}$ while the proportional gains ($K_{\phi}, K_{\delta}, K_{\psi}$) are measured in $\text{kgm}^2 \text{s}^{-1}$. The torque feedback gain $K_{T_{\delta}}$ is dimensionless.

Forward Speed	Feedback On		Feedback Off		Feedback Off (experimental)		
	Value	$D (10^{-4})$	Value	$D (10^{-4})$	Value	$D (10^{-4})$	
2.8 ms^{-1}	$K_{\dot{\phi}}$	-68.53	10.28	-14.93	2.10	-28.19	
	$K_{\dot{\delta}}$	2.09	2.54	2.30	0.24	2.65	
	K_{ϕ}	-146.29	75.99	-16.98	14.54	-79.20	
	K_{δ}	22.18	20.18	4.62	4.98	10.51	
	K_{ψ}	-40.34	12.73	-3.78	5.16	-14.53	
	$K_{T_{\delta}}$	3.52	1.48	-	-	2.59	
	VAF_{ϕ}	81.15		69.61		80.01	
	VAF_{δ}	93.43		23.34		66.84	
	VAF_{ψ}	93.78		69.67		83.30	
3.6 ms^{-1}		Value	$D (10^{-4})$	Value	$D (10^{-4})$	Value	$D (10^{-4})$
	$K_{\dot{\phi}}$	-51.02	16.35	-15.40	4.81	-21.25	5.60
	$K_{\dot{\delta}}$	2.50	7.26	2.81	0.71	2.79	0.09
	K_{ϕ}	-120.51	87.65	-22.82	24.13	-76.41	63.12
	K_{δ}	16.58	38.96	3.94	23.42	17.14	12.36
	K_{ψ}	-43.06	27.15	-7.37	16.00	-13.30	14.25
	$K_{T_{\delta}}$	3.42	1.35	-	-	3.09	0.14
	VAF_{ϕ}	82.85		79.48		73.14	
	VAF_{δ}	91.63		53.29		52.83	
	VAF_{ψ}	95.10		84.88		71.58	
4.7 ms^{-1}		Value	$D (10^{-4})$	Value	$D (10^{-4})$	Value	$D (10^{-4})$
	$K_{\dot{\phi}}$	-51.78	21.61	-19.26	235.55	-14.88	4.65
	$K_{\dot{\delta}}$	2.75	7.09	4.42	85.20	3.04	0.13
	K_{ϕ}	-136.22	150.61	-27.02	33.76	-48.91	65.70
	K_{δ}	3.21	428.40	0.01	345508.59	16.01	15.78
	K_{ψ}	-64.43	49.44	-14.29	243.82	-10.82	15.45
	$K_{T_{\delta}}$	3.70	1.51	-	-	2.61	0.24
	VAF_{ϕ}	77.86		71.14		63.73	
	VAF_{δ}	81.63		36.19		15.61	
	VAF_{ψ}	90.32		80.57		55.71	
5.7 ms^{-1}		Value	$D (10^{-4})$	Value	$D (10^{-4})$	Value	$D (10^{-4})$
	$K_{\dot{\phi}}$	-46.44	73.26	-19.65	24.15	-10.10	3.92
	$K_{\dot{\delta}}$	1.71	388.33	5.42	8.93	3.08	0.14
	K_{ϕ}	-148.46	169.31	-33.34	46.14	-30.95	55.37
	K_{δ}	0.01	79739.10	0.01	87453.73	18.46	11.72
	K_{ψ}	-70.72	53.32	-19.20	64.31	-8.17	14.13
	$K_{T_{\delta}}$	4.34	15.98	-	-	2.58	0.18
	VAF_{ϕ}	70.11		70.08		49.58	
	VAF_{δ}	81.41		40.64		0	
	VAF_{ψ}	80.93		79.50		39.90	

Table 2.3: Results for the final model as estimated for the median rider for all speed levels. Results are presented for the three conditions. Feedback on includes torque feedback in the loop while feedback off completely removes it. Feedback off (experimental) is the model response with all loops connected but with the dynamics of the plant modified to simulate the feedback off condition in the experimental setup. The values of the gains are presented as well as their corresponding uncertainty level measured by the index of dispersion D_i . Additionally, the variance accounted for of the orientation outputs between parametric and non parametric signals is also presented. The derivative gains ($K_{\dot{\phi}}, K_{\dot{\delta}}$) are measured in $\text{kgm}^2 \text{s}^{-2}$ while the proportional gains ($K_{\phi}, K_{\delta}, K_{\psi}$) are measured in $\text{kgm}^2 \text{s}^{-1}$. The torque feedback gain $K_{T_{\delta}}$ is dimensionless.

Forward Speed	Feedback On		Feedback Off		Feedback Off (experimental)	
	Value	$D (10^{-4})$	Value	$D (10^{-4})$	Value	$D (10^{-4})$
2.8 m s^{-1}	$K_{\dot{\phi}}$	-117.66	250.22	-21.12	2.04	-136.89
	$K_{\dot{\delta}}$	3.53	6.11	2.59	0.09	10.89
	K_{ϕ}	-249.69	559.45	-23.98	15.73	-249.15
	K_{δ}	47.65	108.84	4.38	7.65	23.38
	K_{ψ}	-94.92	220.76	-8.72	2.84	-97.57
	$K_{T_{\delta}}$	5.29	14.84	-	-	10.13
	VAF_{ϕ}	78.78		82.85		80.42
	VAF_{δ}	98.22		71.52		97.63
	VAF_{ψ}	94.02		91.91		94.87
3.6 m s^{-1}	$K_{\dot{\phi}}$	-104.10	980.59	-20.03	2.91	-129.91
	$K_{\dot{\delta}}$	7.55	47.00	3.28	0.31	17.90
	K_{ϕ}	-249.90	2435.28	-32.88	22.66	-249.87
	K_{δ}	55.72	545.34	6.79	11.61	35.95
	K_{ψ}	-125.96	1301.09	-15.64	7.05	-133.62
	$K_{T_{\delta}}$	4.53	67.19	-	-	9.89
	VAF_{ϕ}	81.64		86.19		83.39
	VAF_{δ}	98.02		80.82		97.11
	VAF_{ψ}	96.21		97.09		97.15
4.7 m s^{-1}	$K_{\dot{\phi}}$	-121.67	209.42	-25.17	7.62	-165.70
	$K_{\dot{\delta}}$	5.73	7.60	4.27	1.41	24.23
	K_{ϕ}	-249.97	489.65	-35.91	30.85	-249.99
	K_{δ}	37.93	90.56	4.18	80.34	16.79
	K_{ψ}	-216.34	437.41	-28.64	17.11	-239.64
	$K_{T_{\delta}}$	4.91	11.72	-	-	13.14
	VAF_{ϕ}	79.31		82.12		81.73
	VAF_{δ}	97.04		71.92		96.35
	VAF_{ψ}	93.20		95.95		94.65
5.7 m s^{-1}	$K_{\dot{\phi}}$	-108.75	162.97	-28.45	7.54	-150.13
	$K_{\dot{\delta}}$	6.55	16.93	5.57	1.29	31.94
	K_{ϕ}	-228.80	426.18	-40.31	28.94	-221.26
	K_{δ}	31.61	167.83	3.57	143.50	26.49
	K_{ψ}	-241.88	421.73	-41.89	22.39	-248.79
	$K_{T_{\delta}}$	4.79	11.34	-	-	14.61
	VAF_{ϕ}	81.26		83.31		84.26
	VAF_{δ}	97.06		75.79		94.66
	VAF_{ψ}	92.81		96.05		95.50

Parameter	Symbol	Value
wheel base	w	$1.03m$
trail	c	$0.0665m$
steer axis tilt ($\pi/2 - \text{head angle}$)	λ	$\pi/10$
rear wheel	R	
radius	r_R	$0.6858m$
mass	m_R	$8.5 kg$
mass moment of inertia	$(I_{R_{xx}}, I_{R_{yy}})$	$(0.095625, 0.19125) kg m^2$
rear body and frame assembly	B	
position centre of mass	(x_B, z_B)	$(0.4, -0.6)$
mass	m_B	$95kg$
mass moment of inertia	$\begin{bmatrix} I_{B_{xx}} & 0 & I_{B_{xz}} \\ 0 & I_{B_{yy}} & 0 \\ I_{B_{xz}} & 0 & I_{B_{zz}} \end{bmatrix}$	$\begin{bmatrix} 9.2 & 0 & 2.4 \\ 0 & 11 & 0 \\ 2.4 & 0 & 2.8 \end{bmatrix} kg m^2$
front handlebar and fork assembly	H	
position centre of mass	(x_H, z_H)	$(0.9, -0.66)$
mass	m_H	$1.5kg$
mass moment of inertia	$\begin{bmatrix} I_{H_{xx}} & 0 & I_{H_{xz}} \\ 0 & I_{H_{yy}} & 0 \\ I_{H_{xz}} & 0 & I_{H_{zz}} \end{bmatrix}$	$\begin{bmatrix} 0.05892 & 0 & -0.00756 \\ 0 & 0.06 & 0 \\ -0.00756 & 0 & 0.00708 \end{bmatrix} kg m^2$
front wheel	F	
radius	r_F	$0.6858m$
mass	m_F	$1.84kg$
mass moment of inertia	$(I_{F_{xx}}, I_{F_{yy}})$	$(0.097, 0.195) kg m^2$
battery rack	b	
position centre of mass	(x_b, z_b)	$(0.4, -0.55)$
mass	m_b	$4kg$
mass moment of inertia	$\begin{bmatrix} I_{H_{xx}} & 0 & I_{H_{xz}} \\ 0 & I_{H_{yy}} & 0 \\ I_{H_{xz}} & 0 & I_{H_{zz}} \end{bmatrix}$	$\begin{bmatrix} 0.02 & 0 & -0.02 \\ 0 & 0.04 & 0 \\ -0.02 & 0 & 0.02 \end{bmatrix} kg m^2$

Table 2.4: Whipple model parameters for the steer-by-wire bicycle shown in figure.

A

CALIBRATION OF INERTIAL MEASUREMENTS

The fixed body angular velocities measured by the Inertial Measurement Unit (IMU) are biased due to the imperfect orientation of the sensor axis (see figure A.1). The goal is it to align system xyz with the global coordinate system XYZ. To achieve this the euler angle offsets are calculated by using the measurements from MPU-9050's built in accelerometer.

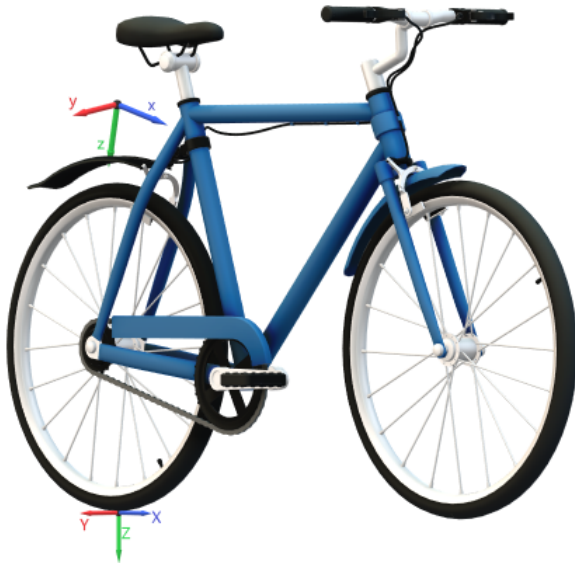


Figure A.1: Bicycle with body fixed sensor axis x-y-z (B) and global axis XYZ (G).

Different orders of rotation affects the end configuration. For this study the intrinsic order Z-Y'-X'' is adopted which is equivalent to the extrinsic X-Y-Z (roll-pitch-yaw). The inverse rotation matrix that described the above rotation sequence is :

$$R_{xyz} = R_x(\phi)R_y(\theta)R_z(\psi) = \begin{pmatrix} \cos\theta \cos\psi & \cos\theta \sin\psi & -\sin\theta \\ \cos\psi \sin\theta \sin\phi - \cos\phi \sin\psi & \cos\phi \cos\psi + \sin\theta \sin\phi \sin\psi & \cos\theta \sin\phi \\ \cos\phi \cos\psi \sin\theta + \sin\phi \sin\psi & \cos\phi \sin\theta \sin\psi - \cos\psi \sin\phi & \cos\theta \cos\phi \end{pmatrix} \quad (\text{A.1})$$

(a) Configuration $i = 1$ (b) Configuration $i = 2$

Figure A.2: a) The bicycle's desired Z axis is aligned with the vector of gravitational acceleration. The bike was validated to be completely upright by the use of a calibrated commercial IMU (MTw Awinda). b) The bicycle's desired X axis is aligned with the vector of gravitational acceleration. The door was validated to be completely vertical by the use of a calibrated commercial IMU (MTw Awinda). \mathbf{g} is the vector measured by the accelerometer which oposite to the gravitational acceleration.

where ϕ is the angle of rotation around axis X, θ is the angle of rotation around axis Y and ψ is the angle of rotation around axis Z. Equation (A.1) maps a vector from the global system G to the body fixed system B. In order to estimate the euler angle offsets the bike was configured in two different ways to align the gravity vector with the z and x axis respectively. The readings from the accelerometer are expressed in the sensor frame (B). Equation (A.2) is used to solve for the euler angle offsets. Unfortunately the three equations have only two degrees of freedom so two configurations are required so as to solve for all three angles.

In the first, $i = 1$ and $\mathbf{g}_1 = [0 \ 0 \ 1]^T$ (see figure A.2a) (note that the vector of accelerations is normalized) with equation (A.2) solving for θ and ϕ . The lack of any dependence on the yaw angle is intuitive to understand since a rotation around the z-axis is aligned with the gravitational field and accelerometers are completely insensitive to rotations about the gravitational field vector. Consequently in the second, $i = 2$ and $\mathbf{g}_2 = [-1 \ 0 \ 0]^T$ which leads to equation (A.2) solving for ψ and θ (see figure A.2b).

$$\frac{\mathbf{G}_i^B}{\|\mathbf{G}_i^B\|} = \begin{pmatrix} G_{ix}^B \\ G_{iy}^B \\ G_{iz}^B \end{pmatrix} \frac{1}{\sqrt{G_{ix}^{B^2} + G_{iy}^{B^2} + G_{iz}^{B^2}}} = \mathbf{R}_{xyz(\phi_o, \theta_o, \psi_o)} \mathbf{g}_i \quad (\text{A.2})$$

Solving equation (A.2) for the angles we get :

$$\phi_o = \tan^{-1} \left(\frac{G_{1y}^B}{G_{1z}^B} \right) \quad (\text{A.3})$$

$$\theta_o = \tan^{-1} \left(\frac{G_{1x}^B}{\sqrt{G_{1y}^B{}^2 + G_{1z}^B{}^2}} \right) \quad (\text{A.4})$$

$$\psi_o = \tan^{-1} \left(\frac{-G_{2y}^B}{\sqrt{G_{2x}^B{}^2 + G_{2z}^B{}^2}} \right) \quad (\text{A.5})$$

From equations (A.3) to (A.5) the euler angle offsets calculated are inserted into rotation matrix R_{xyz} . The transpose of the result (A.6) is then used to transform the IMU measurements from the coordinate frame B to the coordinate frame G which is consistent with the linearized equations of motion defined in ??.

$$R_{IMU} = R_{xyz}^T(\phi_o, \theta_o, \psi_o) = \begin{pmatrix} 0.9939 & -0.006106 & -0.1105 \\ 0.006069 & 1.0 & -0.000675 \\ 0.1105 & 0 & 0.9939 \end{pmatrix} \quad (\text{A.6})$$

B

ORIENTATION ESTIMATION FROM INERTIAL MEASUREMENTS

In order to properly assess the state of the bicycle when comparing it with the Whipple model, measurements of roll angle ϕ and yaw angle ψ are necessary. However the steer-by-wire bicycle has no way of measuring either. For this reason an estimation method is required that can approximate these angles by using measurements from already existing Inertial sensors. A distinction is made between methods that can estimate the euler angles when the whole signal is available for processing and for methods that can produce real-time estimation.

B.1. OFFLINE ESTIMATION METHODS

An estimation of the roll and yaw angle can be made by using the angular rates measured by the gyroscope. However euler angle rates and angular velocities are not equivalent as the former are dependant on order of rotation while the latter are a vector expressed in the body frame. For this reason an expression needs to be formulated that connects the two. Since the euler angle rates are expressed in the local frame of that particular rotation sequence, appropriate rotation matrices need to be used to transform them into vectors in the final body fixed frame (B). The order of rotation used here is the intrinsic X-Y'-Z" (roll-pitch-yaw).

$$\begin{pmatrix} {}^B\omega_x \\ {}^B\omega_y \\ {}^B\omega_z \end{pmatrix} = \begin{pmatrix} 0 \\ 0 \\ \dot{\psi} \end{pmatrix} + {}^B R_G \begin{pmatrix} 0 \\ \dot{\theta} \\ 0 \end{pmatrix} + {}^B R_G {}^G R_F \begin{pmatrix} \dot{\phi} \\ 0 \\ 0 \end{pmatrix} \quad (\text{B.1})$$

where ${}^B\omega_x, {}^B\omega_y, {}^B\omega_z$ the angular rates measured by the gyroscope and F, G the local coordinate systems after the first and second rotation respectively. Note that these measurements are corrected for the imperfect orientation of the IMU sensor by transforming with matrix R_{IMU} (see equation (A.6))

$$\begin{pmatrix} {}^B\omega_x \\ {}^B\omega_y \\ {}^B\omega_z \end{pmatrix} = \begin{pmatrix} 1 & 0 & -\sin\theta \\ 0 & \cos\phi & \cos\theta \sin\phi \\ 0 & -\sin\phi & \cos\phi \cos\theta \end{pmatrix} \begin{pmatrix} \dot{\phi} \\ \dot{\theta} \\ \dot{\psi} \end{pmatrix} \quad (\text{B.2})$$

Simply solving equation (B.2) for the euler angle rates yields the expressions that can be used to calculate the roll and yaw rates from gyroscope measurements.

$$\dot{\phi} = ({}^B\omega_y \sin\phi + {}^B\omega_z \cos\phi) \tan\theta + {}^B\omega_x \approx {}^B\omega_x \quad (\text{B.3})$$

$$\dot{\psi} = \frac{{}^B\omega_y \sin\phi + {}^B\omega_z \cos\phi}{\cos\theta} \approx {}^B\omega_y \sin\phi + {}^B\omega_z \cos\phi \quad (\text{B.4})$$

The newly calculated euler angle rate signals can now be numerically integrated to produce the corresponding euler angles. However, a way needs to be found to account for the accumulating integration error. When the whole signal is available, which is true only in offline (post-processing) applications, two methods were tested for approximating euler angles. The first method removes the drift simply through the use of a high-pass filter. All frequency content under 0.05 Hz is filtered. The second method, removes the drift by subtracting the resulting line from a linear regression. Worth noting here that for the yaw angle this will produce good approximations only when the median of the true signal is around zero, which was mostly true since the subjects tried to keep straight heading in order to avoid falling outside the boundaries of the bicycle lane. For the roll angle this assumptions is confidently made since the signal is expected to be centered around zero. The disadvantage of the high-pass filter was that magnitudes of signals are slightly attenuated, while the disadvantage of the linear regression detrending is that a bias can be introduced if the median is not zero.

B.2. ONLINE ESTIMATION METHODS

With no prior knowledge of the resulting drift another method needs to be found to correct the integration output. Fortunately there are existing ways with which two unreliable sources of a signal can be combined in order to produce a more reliable one. For this a secondary source of pseudo measurements is needed.

My first naive implementation was to calculate the roll from the accelerometer data by assuming that gravity is the only force captured in the accelerometer readings. The formulation of the estimators is identical to the equation (A.3). However, this is not ideal for the particular application of single track vehicles since lateral accelerations due to centrifugal forces heavily change the accelerometer measurements.

Sanjurjo et al. [15] used equations B.5 and B.6 as pseudo absolute measurements. Note that B.6 is directly derived from the second equation of B.2. They explain that equation B.5 is more reliable for angles close to zero and equation B.6 is more reliable for larger roll angles, for this reason a weighted sum of the two methods is employed B.7 that follows the weighting function B.8 .

$$\phi_d = \tan^{-1} \left(\frac{\omega_z^B v}{g} \right) \quad (\text{B.5})$$

$$\phi_\omega = \tan^{-1} \left(\frac{\omega_y^B}{\omega_z^B} \right) \quad (\text{B.6})$$

$$\phi_m = W\phi_d + (1 - W)\phi_\omega \quad (\text{B.7})$$

$$W = \exp \left(-\frac{\hat{\phi}^2}{\bar{\phi}^2} \right) \quad (\text{B.8})$$

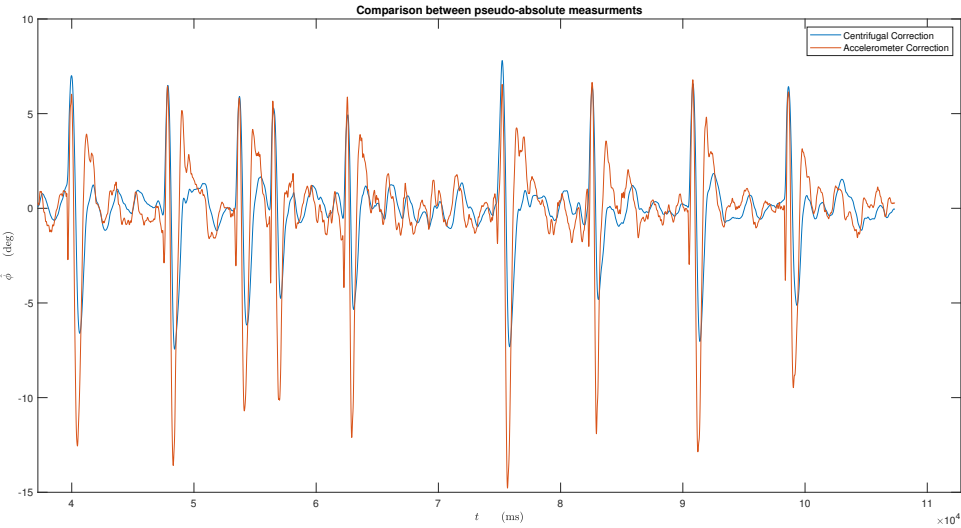
where W is the weighting function, $\hat{\phi}$ is the last available estimation of roll and $\bar{\phi}^2$ is a constant that can be used to adjust the weighting function. Sanjuro et al. used $\bar{\phi}^2 = 0.05$.

For the sensor fusion algorithm both a simple complimentary filter and a Kalman filter were tested. The complementary filter works by combining the desirable low-frequency characteristics of the absolute measurements with the desirable high-frequency characteristics of the euler integration output.

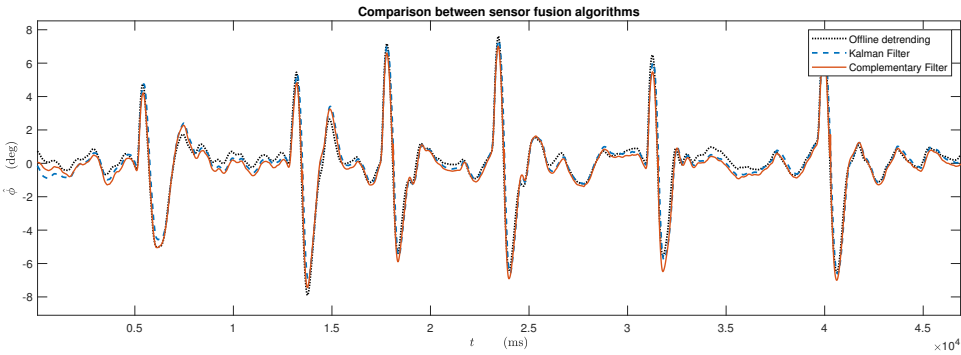
$$\hat{\phi}_k = (1 - \alpha) \cdot (\hat{\phi}_{k-1} + {}^B\omega_{x,k} \cdot dt) + \alpha \cdot \phi_m \quad (\text{B.9})$$

where k is the current iteration of the microcontroller and α is a constant, such that $0 < \alpha < 1$. The larger the α , the more pseudo absolute measurements are 'trusted'. As α goes to zero the estimate is mainly based on the integration output.

On the other hand, Kalman filters are also often used as state estimators when multiple measurement sources need to be combined into a single more reliable one. Often the output of a model is combined with absolute measurements and an estimation of the state is made by dynamically weighting the two sources of information. In this case a simple plant model is created which has $\dot{\phi} \approx {}^B\omega_x$ as input and produces the roll angle of the next time step given the previous one. In order to account for biases in the angular rate sensor an extra



(a) Comparison between pseudo-absolute measurements



(b) Comparison between sensor fusion algorithms

Figure B.1: a) Comparison between pseudo-absolute measurements. Both sources were fused with the integration output via a Kalman filter. The blue line is the result of the measurements used by Sanjurjo et al. [15] while the orange line is the result of the estimation produced using the accelerometer equation (A.3). b) Comparison between sensor fusion algorithms. For reference the output of the offline linear regression detrending is shown as a black dotted line.

state b_x is added to the model. The complete formulation is given by :

$$\begin{bmatrix} \hat{\phi} \\ \hat{b}_x \end{bmatrix}_k^- = \begin{bmatrix} 1 & -dt \\ 0 & 1 \end{bmatrix} \begin{bmatrix} \hat{\phi} \\ \hat{b}_x \end{bmatrix}_{k-1}^+ + \begin{bmatrix} dt \\ 0 \end{bmatrix} {}^B\omega_{x,k-1} \quad (\text{B.10})$$

The results are shown in figure B.1. In figure B.1a it is visible that the naive implementation using the assumption that the accelerometer only registers the gravitational acceleration does not work. However, for the first few seconds after turning on the bike the assumption is correct and a good initial condition estimate can be extracted in order to use as initial condition in the sensor fusion algorithm of choice. As far as the sensor fusion algorithm is concerned the results are shown in figure B.1b. A complimentary filter with $\alpha = 0.0022$ is used, while for the Kalman filter the process covariance matrix and measurement variance were equal to:

$$Q_P = \begin{bmatrix} 9e^{-4} & 0 \\ 0 & 3e^{-4} \end{bmatrix} dt \quad (\text{B.11})$$

$$Q_S = 0.5 \quad (\text{B.12})$$

Additionally the initial covariance matrix was equal to zero which means that the filter at the start "trusts" the model output; the Euler integration output. As a reference the result from the linear regression detrending is

also presented. The graph indicates that both methods successfully approximate the reference result. Furthermore, it is clear that with this general system model, only a slight performance gain (if any) can be gained by using the Kalman filter. Additionally, the implementation of the complimentary filter is far simpler and consequently much less computationally expensive. Had the Kalman filter been implemented on a system where an accurate dynamic model was present, the Kalman filter would – in pretty much all cases – trump the simpler complimentary filter. For this reason the complimentary filter approach was chosen for the on-line implementation of roll estimation in the steer-by-wire bicycle, considering the limiting clock speed of microcontroller Teensy 3.6.

The above pseudo-absolute measurements can only be used to estimate the roll angle. However there is a way to extract an estimation of the yaw relative to the magnetic north by using the magnetometer sensor, which is also part of the IMU. This is similar to how modern smartphones can work as a compass. Similar to how an estimation of the roll angle was made by equating the accelerometer readings with reference position where the gravitational acceleration is completley aligned with the bike's z-axis, the same can be done by equating the magnetometer readings with the reference position of the bike's x axis pointing towards the magnetic north. The magnetometer in this reference position are

$$\mathbf{B}_{ref} = B \begin{pmatrix} \cos \zeta \\ 0 \\ \sin \zeta \end{pmatrix} \quad (B.13)$$

where B is the geomagnetic field strength and ζ is the angle of inclination of the geomagnetic field measured downwards from horizontal. Both values vary over the earth's surface. Detailed geomagnetic field maps are available from the World Data Center for Geomagnetism at <http://wdc.kugi.kyoto-u.ac.jp/igrf/>. Fortunately, both B and ζ cancel out in the final formulation of the estimator.

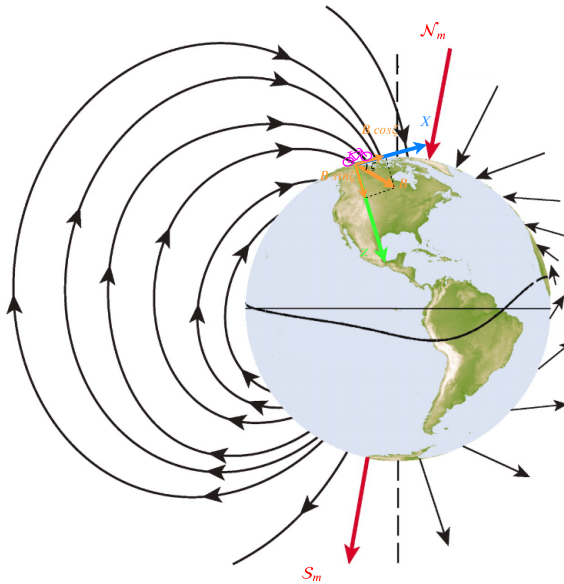


Figure B.2: Magnetic Field vectors in the reference position.

The measured magnetometer readings \mathbf{B}_p after three rotations are described by equations :

$$\mathbf{B}_p = \mathbf{R}_{xyz}(\phi, \theta, \psi) \cdot B \begin{pmatrix} \cos \zeta \\ 0 \\ \sin \zeta \end{pmatrix} + \begin{pmatrix} V_x \\ V_y \\ V_z \end{pmatrix} \quad (B.14)$$

where \mathbf{R}_{xyz} the rotation matrix defined in ??eq:rotmat2) and V_x, V_y, V_z are the components of the Hard-Iron vector, which is a fixed magnetic offset adding to the true magnetometer sensor output. The Hard-Iron offset is the sum of any intrinsic zero field offset within the magnetometer sensor itself plus permanent magnetic

fields within the PCB generated by magnetized ferromagnetic materials. It is quite normal for the Hard-Iron offset to greatly exceed the geomagnetic field. Therefore an accurate Hard-Iron estimation and subtraction are required.

The Hard-Iron offset can be estimated if we consider that the set of all 3d points defined by every magnetometer reading lies in the surface of a sphere with radius B . In the presence of the offset, the center of the sphere would be displaced by the Hard-Iron Vector \mathbf{V} . The components of vector \mathbf{V} can be estimated by fitting the magnetometer measurements to the equation:

$$(\mathbf{B}_p - \mathbf{V})^T (\mathbf{B}_p - \mathbf{V}) = B^2 \quad (\text{B.15})$$

Equation (B.15) was solved with the gradient descend method by minimizing the sum of the squared difference between the right and left hand side of the equation. The resulting Hard-Iron Offset Vector was :

$$\mathbf{V} = \begin{pmatrix} -22.03 & -26.14 & -1.651 \end{pmatrix} \quad [\mu\text{T}] \quad (\text{B.16})$$

In figure B.3 the locus defined by the set of vectors measured by the magnetometer is displayed. It is visible that after the correction the measurements lie on the surface of a sphere with center in the origin and radius approximately equal to 1 a.u.

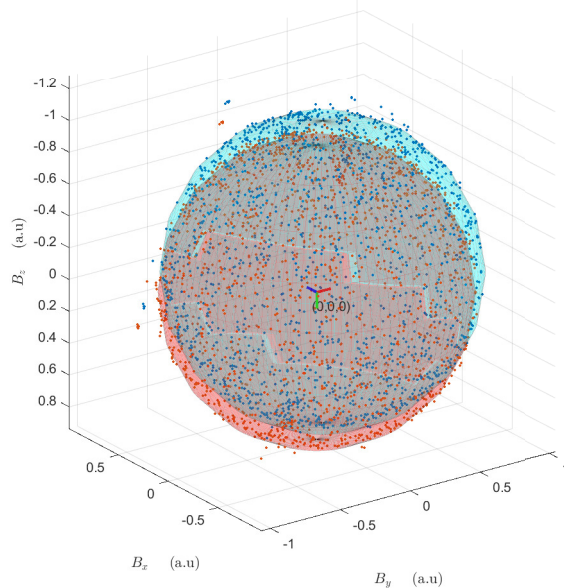


Figure B.3: The blue dots are the locus of the magnetometer readings before correcting for the hard iron offset. The red dots are the locus of the magnetometer readings after correcting for the offset. The magnetometer readings have been normalized so that 1 a.u = 49.0913 μT which is the Magnetic Field Intensity for the approximate location of TU Delft (Latitude 52° 0' 0" N and Longitude: 4° 22' 0" E).

Having estimated \mathbf{V} from equation (B.14) by assuming $\theta \approx 0$ we get :

$$\mathbf{B}_f = \mathbf{B}_p - \mathbf{V} = \mathbf{R}_x(\phi)\mathbf{R}_z(\psi) \cdot \begin{pmatrix} B \cos \zeta \\ 0 \\ B \sin \zeta \end{pmatrix} \quad (\text{B.17})$$

$$\mathbf{R}_x^T(\phi) \begin{pmatrix} B_{fx} \\ B_{fy} \\ B_{fz} \end{pmatrix} = \begin{pmatrix} \cos \psi B \cos \delta \\ -\sin \psi B \cos \delta \\ B \sin \delta \end{pmatrix} \quad (\text{B.18})$$

$$\begin{pmatrix} B_{fx} \\ B_{fy} \cos \phi - B_{fz} \sin \phi \\ B_{fy} \sin \phi + B_{fz} \cos \phi \end{pmatrix} = \begin{pmatrix} \cos \psi B \cos \delta \\ -\sin \psi B \cos \delta \\ B \sin \delta \end{pmatrix} \quad (\text{B.19})$$

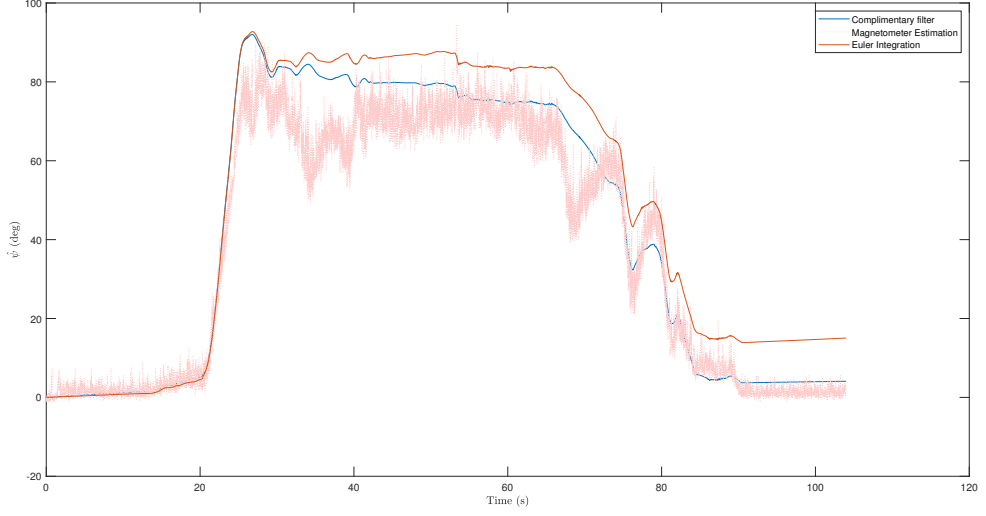


Figure B.4: Comparison of online yaw angle estimation. Red dotted line is the pure estimation from the magnetometer data. Orange line is the drifted euler integration output. Blue line is the result of the complimentary filter sensor fusing the other two signals. For the complimentary filter $a = 0.00027$.

By dividing the y and x component of equation (B.19) we get:

$$\hat{\psi} = \tan^{-1} \left(\frac{B_{fx} \sin \hat{\phi} - B_{fy} \cos \hat{\phi}}{B_{fx}} \right) \quad (\text{B.20})$$

where $\hat{\phi}$ is the estimate of roll angle obtained from the aforementioned methods. Equation (B.20) can now be used as a source of pseudo-absolute measurements for the sensor fusion algorithm of choice. Regarding signal fusion the same things apply as in the roll angle estimation case. Finally since we want the yaw angle relative to the starting position and not relative to the magnetic north the value of the first yaw estimation is subtracted from all subsequent computations.

C

ESTIMATION OF RIDER TORQUE

Given the steer rate ($\dot{\delta}$) and acceleration ($\ddot{\delta}$), moment of inertia (I_H), motor damping (b_m) and the torque applied by the handlebar motor (T_{PDH}) the equation of motion of the upper handlebar assembly can be formed (see Fig. C.1) and solved for the unknown rider input torque (T_H).

$$T_H = \ddot{\delta} I_H + \dot{\delta} b_m - T_{PDH} \quad (\text{C.1})$$

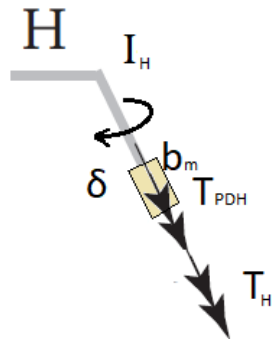


Figure C.1: Free body diagram of the upper handlebar assembly.

C.1. STEER RATE AND ACCELERATION

Since only the steering angle is directly measurable, a way needs to be found that produces accurate estimations of steer rate and steer acceleration. Simple numerical differencing techniques proved ineffective as noise effects were magnified resulting in corrupted second derivatives, even after filtering the original signal to a cutoff frequency of 10 Hz.

To combat this problem a piecewise cubic interpolation technique using the cubic spline function was used. The principle of this method is simple. Third order polynomials are fitted between the datapoints. This results in a signal that is identical to the original but instead of discrete points, it is represented by the union of polynomial functions. After this point the steer rate and acceleration can be easily obtained by taking the derivatives of the polynomials. the result of the method is seen in figure C.2.

C.2. STEERING SHAFT MOMENT OF INERTIA AND VISCOUS FRICITION

In order to make estimation of applied rider torque, the damping coefficient and the inertia of the steering shaft needs to be determined. There are multiple ways to measure inertia of complex geometries. Here an

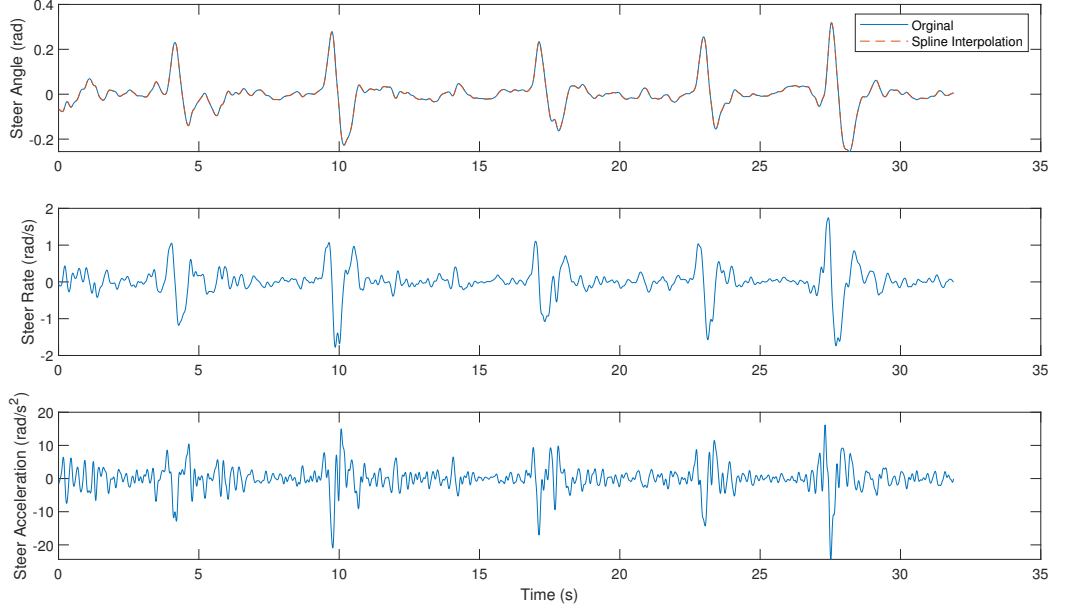


Figure C.2: Steering angle signal with its derivates produced by the piecewise cubic spline interpolation method.

estimation through a simple experimental setup is chosen.

By connecting the steering shaft with two extension springs (see Fig.C.3) and measuring the oscillations of the steering angle δ , a mechanical system is created where it has to obey equation C.2.

$$I_H \ddot{\delta}(t) + b_m \dot{\delta}(t) + 2K\alpha^2 \delta(t) = 0 \quad (\text{C.2})$$

where K the spring elastic constant and α the moment arm shown in figure C.3.

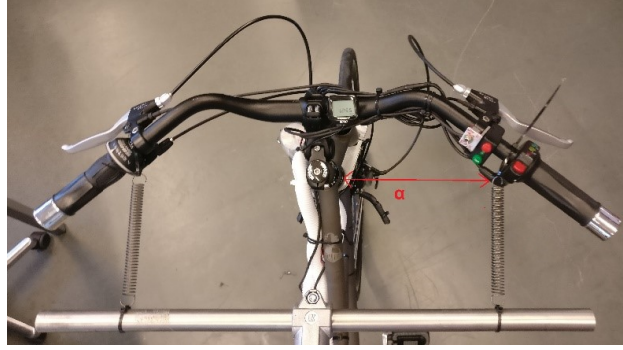


Figure C.3: Spring-handlebar assembly where α is the moment arm.

The springs ($K = 555 \text{ N/m}$ and slack length of 0.03 m) are attached to the handlebar and the system is perturbed. The measured steering angle signal from one of the perturbation tests is shown in figure C.4. The steering rate and acceleration signals are derived by the methods described in section C.1. Equation C.2 is then applied to all discrete time steps and so the system of equations C.3 is created.

$$\begin{bmatrix} \ddot{\delta}_1 & \dot{\delta}_1 \\ \ddot{\delta}_2 & \dot{\delta}_2 \\ \vdots & \vdots \\ \ddot{\delta}_N & \dot{\delta}_N \end{bmatrix} \begin{bmatrix} I_H \\ b_m \end{bmatrix} = -2K\alpha^2 \begin{bmatrix} \delta_1 \\ \vdots \\ \delta_N \end{bmatrix} \quad (\text{C.3})$$

where N the length of the recorded signal.

Since equation C.3 is linear in the parameters, the solution of the regression problem can be approximated by the use of the least squares method.

$$\begin{bmatrix} I_H \\ b_m \end{bmatrix} = -2K\alpha^2 \left(\begin{bmatrix} \ddot{\delta}_1 & \dot{\delta}_1 \\ \ddot{\delta}_2 & \dot{\delta}_2 \\ \vdots & \vdots \\ \ddot{\delta}_N & \dot{\delta}_N \end{bmatrix}^T \begin{bmatrix} \ddot{\delta}_1 & \dot{\delta}_1 \\ \ddot{\delta}_2 & \dot{\delta}_2 \\ \vdots & \vdots \\ \ddot{\delta}_N & \dot{\delta}_N \end{bmatrix} \right)^{-1} \begin{bmatrix} \ddot{\delta}_1 & \dot{\delta}_1 \\ \ddot{\delta}_2 & \dot{\delta}_2 \\ \vdots & \vdots \\ \ddot{\delta}_N & \dot{\delta}_N \end{bmatrix}^T \begin{bmatrix} \delta_1 \\ \dots \\ \delta_N \end{bmatrix} \quad (\text{C.4})$$

The system is perturbed 15 times so 15 sets of inertia and damping ratios are computed. The mean of the these was taken and resulted in $I_H = 0.0960 \text{ kg m}^2$ and $b_m = 0.2663 \text{ N s}^{-1}$

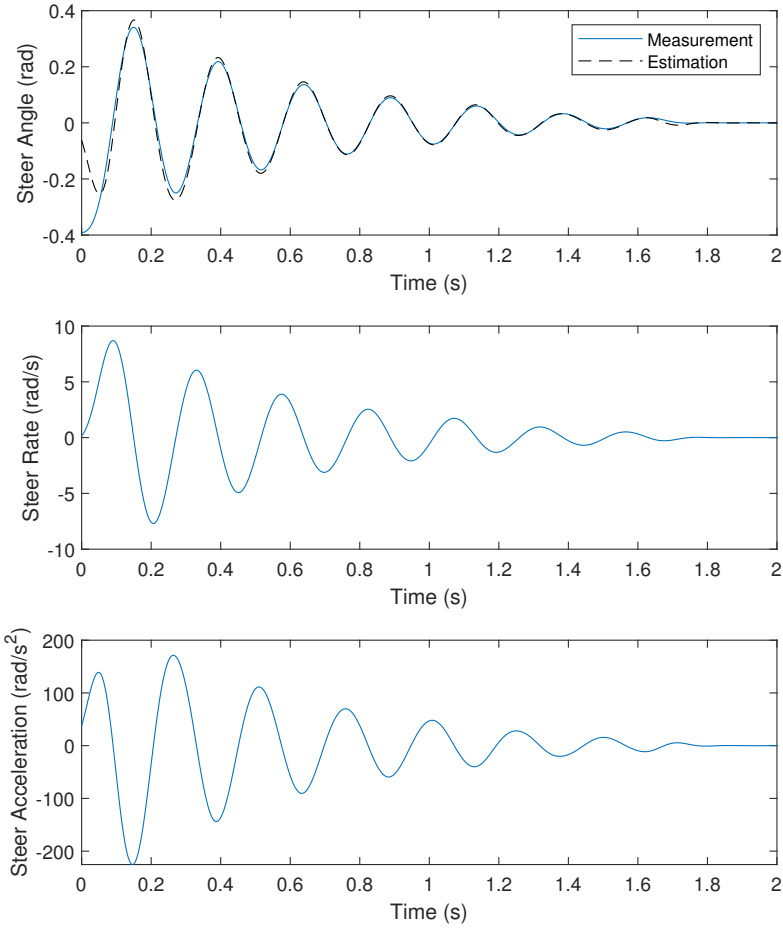


Figure C.4: Result of the first of fifteen oscillations. Blue lines indicate the measured signals while the black dotted line is the output of the model given the values of inertia and damping estimated with the least squares method.

C.3. MOTOR TORQUE INPUT VALIDATION

C.3.1. DESIGN OF TORQUE SENSOR

In order to validate that the torque exerted by the handlebar motor results in equivalent input rider torque a torque sensor is designed and attached to the steering shaft. The most common torque sensor measurement principle uses bonded strain gauge technology, where the strain gauges are bonded to a suitably designed shaft.

In the torsion of a cylindrical shaft the strain is measured by the angle of twist or angular deflection. Unfortunately stain gauges can only detect compressive and tensile strain. The strain gauges are placed with such an orientation that the shearing stress is replaced by its equivalent principal stresses. The angle and the magnitude of the principal stresses are calculated by the use of the Mohr Circle. In this case the principal tension and compressive stresses are of the same magnitude as the shearing stress and are active at an angle of 45 degrees since it is considered that no external compressive or tension force is present.

In order to design a proper cylindrical shaft for the torque sensor the diameter of the shaft is chosen such that the strain measured in the strain gauges is within the detectable range ($\epsilon_{min} = 10^{-5}$, $\epsilon_{max} = 6 \cdot 10^{-4}$). For this application, a hollow cylindrical shaft made of aluminum (AL7075 – O) is used so the unknowns are the inner and outer diameters. The strain is given in relation to the stress by Hooke's law for isotropic materials by equation (C.5). The shearing stress is in turn given by equation (C.6).

$$\epsilon = \frac{\sigma \cdot (1 + \nu)}{E} \quad (C.5)$$

where ν the Poisson's ratio and E the Young's Modulus (Pa)

$$\tau = \frac{T \cdot r}{J} \quad (C.6)$$

where J is the polar moment of inertia (m^4), r the distance from center to stressed surface in the given position (mm), T the twisting moment (Nm). The polar moment of inertia of a circular hollow shaft can be expressed as

$$J = \frac{\pi \cdot (D^4 - d^4)}{32} \quad (C.7)$$

where d is shaft inside diameter (mm) and D is the shaft outside diameter (mm).

By inputting the above equations into a MATLAB script figure C.5 was produced. The figure was created for a fixed inner diameter of 12mm, due to limitations in the machining process. It is evident that the lower the width of the shaft the higher detection of the low level torques. For this reason a width of 2 mm was chosen. This still means that torques below 0.2Nm are not detectable. However the purpose of the torque sensor is not to provide accurate online measurements but to validate the input torques from the handlebar motor. The design of the resulting part is shown in C.6.

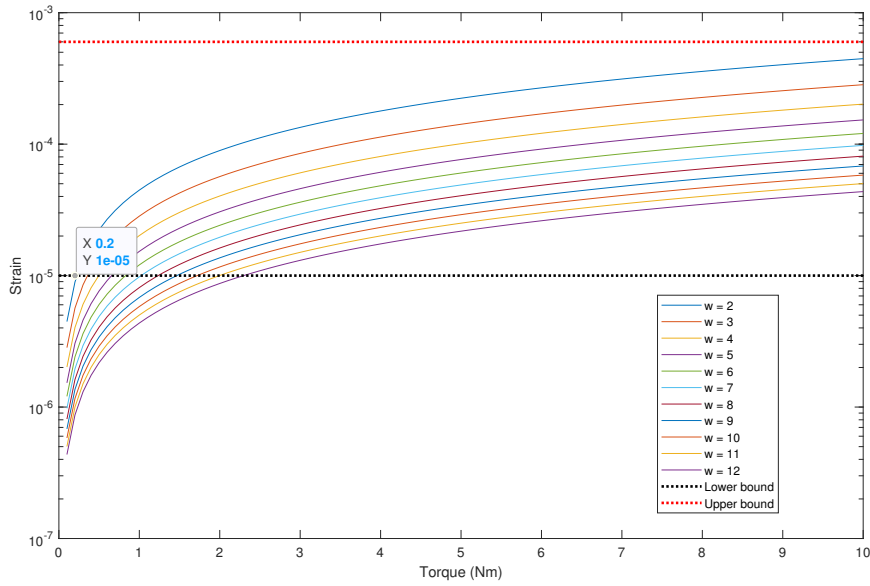


Figure C.5: Principal tensile strain in the 45 degree angle for various shaft widths (w).

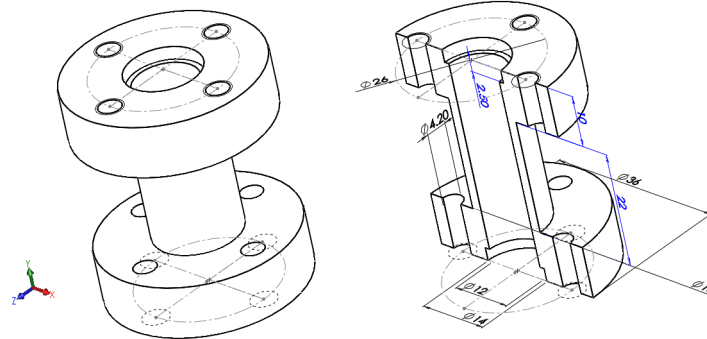


Figure C.6: Schematic of the hollow shaft.

Because it is not an ideal hollow cylinder, the shearing stress calculated analytically from the above equations needs to be validated. A static load simulation in SolidWorks is done to see how much different is the shearing stress on the external surface. As it turns out the simulation showed a shearing stress similar to the one calculated by the equations. In C.7 the simulation results for a loading of 10Nm is shown. For comparison the resulting shearing stress calculated analytically is $10.0874 \cdot 10^6 N/m^2$. For proper measurements of strain the gauge placement should gravitate towards the middle to avoid the spikes of shearing stress near the intersections between the main shaft and the cylindrical heads (see fig. C.7)

C.3.2. RESULTS

In order to validate that the commanded torque in the handlebar motor is the same as the one actually applied in the handlebar, a trial identification run was conducted to simulate steer torque levels of the experiments. The signal of the input motor torque is compared with the output of the custom made torque sensor. The results are shown in figure C.8. The mismatch of the two signals for values lower than 0.5Nm is attributed to the fact that the sensor's strain gauges cannot accurately measure the strain in the material to produce reliable ouput as determined analytically beforehand. Also during the measurements a slight bias of the sensor was noted when $0 < \delta < \pi/2$. Despite the aforementioned, the resulting Variance Accounted For (VAF) was

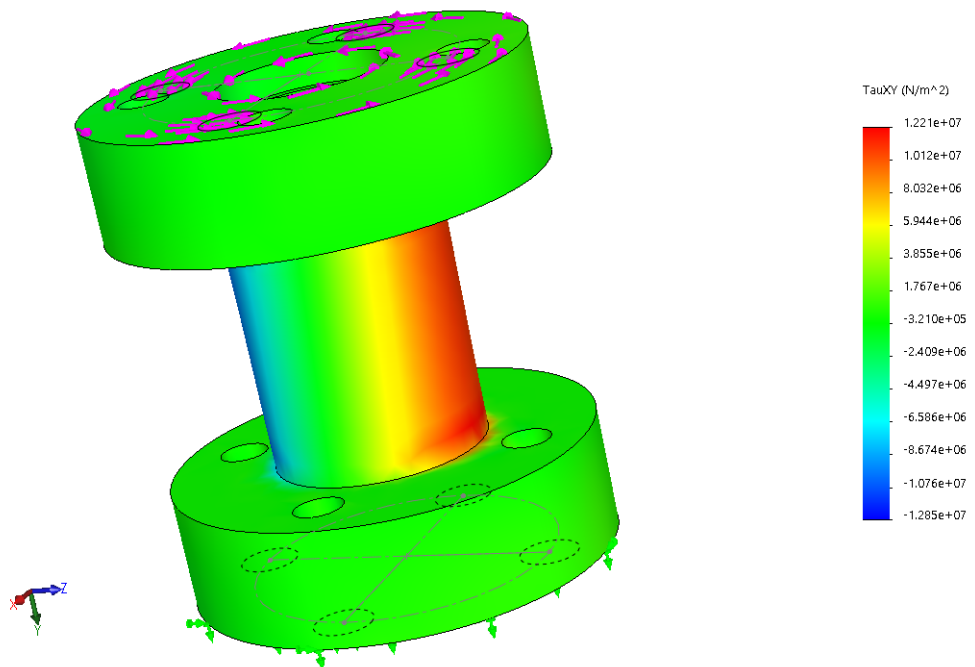


Figure C.7: Shearing stress for 10Nm loading in the axial direction.

equal to 90.77% and was deemed that the motor command torque is indeed what is being applied in the steering shaft so in all subsequent calculation it was taken as ground truth.

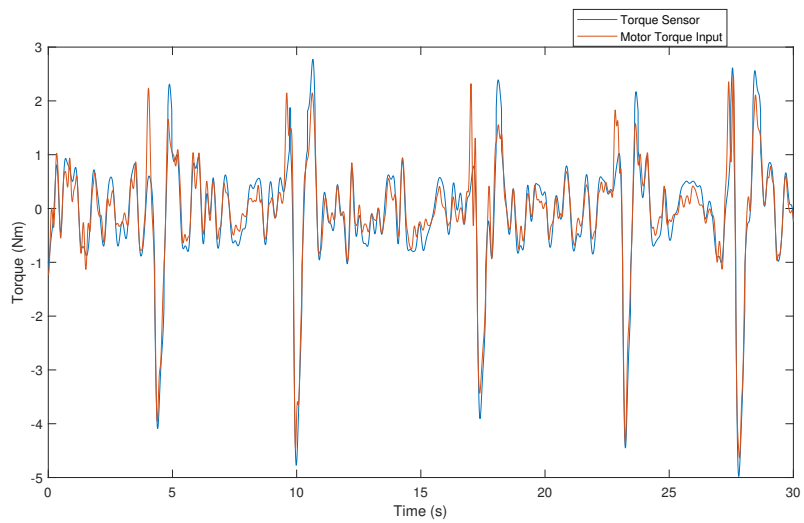


Figure C.8: Measurement of torque sensor compared to the commanded torque of the handlebar motor.

BIBLIOGRAPHY

- [1] Michael Barnett-Cowan. Vestibular perception is slow: a review. *Multisensory research*, 26(4):387–403, 2013.
- [2] Erwin De Vlugt, Alfred C Schouten, and Frans CT Van Der Helm. Adaptation of reflexive feedback during arm posture to different environments. *Biological cybernetics*, 87(1):10–26, 2002.
- [3] Georgios Dialynas, Christos Christoforidis, Riender Happee, and AL Schwab. The effect of haptic feedback in the balance task of bicycling. *Symposium on the Dynamics and Control of Single Track Vehicles*.
- [4] DJ Eaton. *Man-Machine Dynamics in the Stabilization of Single-Track Vehicles*, " Univ. of Michigan. PhD thesis, Ph. D. Thesis, 1975.
- [5] J. W. de Haan Georgios Dialynas. The response of the bicycle rider's body to vertical fore-and-aft and lateral perturbations; experimental tests. *Journal of Mechanical Engineering*, 463(2084):1955–1982, 2007.
- [6] Riender Happee, Erwin De Vlugt, and Alfred C Schouten. Posture maintenance of the human upper extremity; identification of intrinsic and reflex based contributions. *SAE International Journal of Passenger Cars-Mechanical Systems*, 1(2008-01-1888):1125–1135, 2008.
- [7] JDG Kooijman and AL Schwab. A review on bicycle and motorcycle rider control with a perspective on handling qualities. *Vehicle system dynamics*, 51(11):1722–1764, 2013.
- [8] I. Krul, S. Nijman, and C. Stam. Verkeersongevallen 2016, 2016. URL <https://www veiligheid nl/organisatie/over-veiligheidnl/publicaties>.
- [9] Duane T McRuer and Ezra S Krendel. The human operator as a servo system element. *Journal of the Franklin Institute*, 267(5):381–403, 1959.
- [10] Duane T McRuer, Dunstan Graham, and Ezra S Krendel. Manual control of single-loop systems: Part i. *Journal of the Franklin Institute*, 283(1):1–29, 1967.
- [11] Duane T McRuer, Dunstan Graham, and Ezra S Krendel. Manual control of single-loop systems: Part ii. *Journal of the Franklin Institute*, 283(2):145–168, 1967.
- [12] Jaap P Meijaard, Jim M Papadopoulos, Andy Ruina, and Arend L Schwab. Linearized dynamics equations for the balance and steer of a bicycle: a benchmark and review. *Proceedings of the Royal society A: mathematical, physical and engineering sciences*, 463(2084):1955–1982, 2007.
- [13] RC Miall, D Jo Weir, Daniel M Wolpert, and JF Stein. Is the cerebellum a smith predictor? *Journal of motor behavior*, 25(3):203–216, 1993.
- [14] Jason Keith Moore. *Human control of a bicycle*. University of California, Davis Davis, CA, 2012.
- [15] Emilio Sanjurjo, Miguel A Naya, Javier Cuadrado, and Arend L Schwab. Roll angle estimator based on angular rate measurements for bicycles. *Vehicle System Dynamics*, pages 1–15, 2018.
- [16] Frans CT Van der Helm, Alfred C Schouten, Erwin de Vlugt, and Guido G Brouwn. Identification of intrinsic and reflexive components of human arm dynamics during postural control. *Journal of neuroscience methods*, 119(1):1–14, 2002.
- [17] Herman van der Kooij, Ron Jacobs, Bart Koopman, and Frans van der Helm. An adaptive model of sensory integration in a dynamic environment applied to human stance control. *Biological cybernetics*, 84(2):103–115, 2001.
- [18] David H Weir. A manual control view of motorcycle handling. Technical report, 1973.